The value of different reconstruction algorithms for quantification of FDG PET brain imaging

Tumelo Carel Godwin MOALOSI

Dissertation presented in partial fulfilment of the requirements for the degree of Master of Science in Medical Physics in the Faculty of Medicine and Health Sciences, at Stellenbosch University

Supervisor: Prof. Annare Ellmann

Co-supervisors:

Dr. Michael Mix

Prof. James Warwick

Ms. Monique du Toit

Co-investigator: Dr. Alexander Doruyter

December 2016

Declaration

By submitting this thesis electronically, I Tumelo Carel Godwin MOALOSI declare that the entirety of the work contained therein is my own, original work, that I am the sole author thereof, that reproduction and publication thereof by Stellenbosch University will not infringe any third party rights and that I have not previously in its entirety or in part submitted it for obtaining any qualification.

Date: December 2016

Abstract

Modern reconstruction techniques of positron emission tomography/computed tomography (PET/CT) data are optimised for whole body imaging. Such optimisation is less developed for brain imaging. This study aimed at investigating the effect of different image reconstruction parameters (varying number of iterations, scan duration, relaxation parameter (smoothing levels) and the use of time of flight (TOF)) on PET/CT images with the objective of evaluating the algorithms for quantification of fluorodeoxyglucose (FDG) PET brain imaging.

Materials and methods

A Philips® Gemini TF Big Bore PET/CT scanner was used for acquiring the data. The study was based primarily on phantom and limited patient data for preliminary validation. Three dimensional (3D) Hoffman brain phantom (HBP) data and data of patients attending the Western Cape Academic PET/CT Centre for oncological purposes, with low probability of neurological pathology, were included in the study. The data was reconstructed using two different iterative reconstruction algorithms, row action maximum likelihood algorithm (RAMLA) and spherically symmetric basis function ordered subset algorithm (BLOB or BLOB OS), with variation in the number of iterations, scan acquisition duration, switching TOF on and off for BLOB OS and by varying the relaxation parameter. The set of output images were analysed using MATLAB code.

Results

From the HBP data, in all regions of the brain, the grey matter/white matter ratio, and the mean and the normalised mean counts increased as the number of iterations increased, reaching a plateau after 15 iterations for all algorithms. When comparing the algorithms with relaxation values λ=0.7 and λ=1.0, it was found that the latter converged faster. Overall, BLOB TOF (λ=1.0) proved to have faster convergence followed by BLOB TOF (λ=0.7). The coefficient of variation (COV) for all volumes of interest showed BLOB TOF to be superior compared to all the other algorithms. The COV results for different scan durations showed that there is minimal improvement after 5 min in high-activity regions (GM) and after 10 min in low-activity region (WM). The patient data was used as proof of principle but the numbers were too small to analyse further, as no pattern of behaviour could be identified for the different algorithms in the three patient images available.

Conclusions

A higher number of iterations, such as 15, than currently used by the vendor of the PET scanner led to improved image quality for all algorithms. An acquisition time of 10 min provided an optimal trade-off between image quality and scan time irrespective of the reconstruction algorithm used. Including the TOF in the reconstruction algorithm improved the image quality, proving that TOF also improves image quality for small objects such as the brain similar to that seen for larger anatomical diameters as indicated in the literature.

Opsomming

Moderne rekonstruksietegnieke van PET/RT data word geoptimaliseer vir heelliggaambeelding. Sodanige optimalisering is minder ontwikkel vir breinbeelding. Die doel van hierdie studie was om die effek van verskillende beeldrekonstruksieparameters (aantal iterasies, die duur van die skandering, veslappingsparameters (vergladdingsvlakke) en die gebruik van “tyd-van-vlug” (Engels: “time of flight” (TOF)) inligting) met PET/RT te ondersoek, om sodoende die verskillende rekonstruksie-algoritmes vir kwantifisering van FDG PET breinbeelding te evalueer.

Materiaal en Metodes

‘n Philips® Gemini TF Big Bore PET/RT is gebruik om die data te versamel. Die studie het hoofsaaklik fantoom- en beperkte pasiëntdata ingesluit. Data van ‘n 3D Hoffman breinfantoom asook van pasiënte wat die Wes-Kaapse Akademiese PET/RT Sentrum vir onkologiese ondersoeke besoek het en lae waarskynlikhheid vir neurologiese patologie gehad het, is in die studie gebruik. Die data is met twee verskillende iteratiewe rekonstruksie-algoritmes, RAMLA en BLOB OS gerekonstrueer, met variasies in die aantal iterasies, tydsduur van beeldopname, met en sonder TOF vir BLOB OS en met variasie van die verslappingsparameter. Die beelde wat verkry is, is met MATLAB kodes ontleed.

Resultate

Die Hoffman breinfantoomdata het getoon dat die verhouding van grysstof tot witstof (GS/WS) vir alle areas in die brein toegeneem het met ’n toenemende aantal iterasies en vir alle algoritmes na 15 iterasies ‘n plato bereik het. As die algoritmes met verslappingsparameters van λ=0.7 en λ=1.0 vergelyk is, is daar gevind dat (λ=1.0) vinniger as (λ=0.7) konvergeer het. Van al die algoritmes het BLOB TOF(λ=1.0) die vinnigste konvergeer, gevolg deur BLOB TOF (λ=0.7). Die variasiekoëffisiënt (VK) vir alle volumes-van-belang het getoon dat BLOB TOF beter was as die ander algoritmes wat vergelyk is. Die VK resultate vir verskillende beeldingstye het getoon dat daar in hoë aktiwiteitsareas (GS) na 5 min minimale verbetering plaasgevind het, en in lae aktiwiteitsareas (WS) na 10 min. Die pasiëntdata is as bewys van beginsel gebruik, maar die getalle was te klein vir verdere analise, omdat daar geen identifiseerbare patrone vir die verskillende algoritmes in die data van die drie pasiënte was nie.

Gevolgtrekking

Meer iterasies as wat tans deur die verskaffer van die skandeerder gebruik word, byvoorbeeld 15, het tot ’n verbetering in beeldkwaliteit vir al die algoritmes gelei. ‘n Beeldingstyd van 10 min het, onafhanklik van die rekonstruksie-algoritme, ‘n optimale kompromis tussen beeldkwaliteit en beeldingstyd gegee. Die insluiting van TOF in die rekonstruksie-algoritme het bewys dat TOF ook die beeldkwaliteit van klein organe soos die brein verbeter, soortgelyk aan wat met groter anatomiese deursnit voorwerpe ondervind word, soos ook in die literatuur aangedui is.

Acknowledgements

The start and completion of this work seemed impossible but with the support and encouragement from many, the final product is here.

I would like to thank my mentors, co-investigators and supervisors:

Prof. Patrick Dupont (mentor, KU Leuven, Belgium), who is the initiator of this project, for the long hours spent while brainstorming in search of this research idea. His expertise led to the realisation of this work. His scientific analysis tools he made available for this project proved invaluable. Thank you for believing in me. You enthusiastically followed my progress and your encouraging words kept me focused to completion of this project.

The head of Division of Nuclear Medicine and my supervisor, Prof. A Ellmann, to whom I will forever be indebted for the opportunities she placed at my disposal in order to realise the completion of this project and for my development in the field.

Dr. Michael Mix (University Medical Center Freiburg, Germany) for the immense experience he imparted to me and the knowledge he shared, as well as the time he gave in the reconstruction of the data.

Prof. J Warwick, Ms. M du Toit and Dr. A Doruyter for the in-house support and the encouragement in seeing me through this journey.

Thanks to my friends and colleagues:

The staff at the Western Cape Academic PET/CT Centre for the support and assistance during the patient recruitment phase, as well as scanning. You guys rock!!!

The staff of the Medical Physics and Nuclear Medicine Divisions at large.

Special thanks to:

My immediate colleague Ms. L Nolan who always availed herself to cover for me when I was busy with this project.

The registrars who were involved during patient screening, this work would not have had value if it was not for your time.

My friends Dr. X Ndlovu, Dr. J Mugisha, Mr. M Mohlapoli and Mr. T Mkhize who spent many hours proof reading my thesis and sharing their research experiences with me.

Dedications

This work is dedicated to the almighty GOD through whom all things are possible (1 Cor 2:9), my ever supporting and loving wife (Matseki) and son (Lesedi). I thank you for being there for me during my absence and sleepless nights; you always supported me and never doubted my potential.

My family (Boo-ra Moalosi le Ba-ha Rampai) for the moral compass, Ke lebogetse tshegetso ya lona ka megopolo le dithapelo Batshweneng le Bataung ba bantle, this would not have been possible without you. The congregation of the Glory Acts Pentecost Church, your prayers are never without effect and I thank you for that.

Table of Contents

List of Figures

List of Tables

List of Abbreviations

3D	-	three dimensional
ACF	-	attenuation correction factors
ART	-	algebraic reconstruction technique
BGO	-	Bismuth germanate
BLOB OS	-	spherically symmetric basis function ordered subset algorithm
CFOV	-	central field of view
CNS	-	central nervous system
COV	-	coefficient of variation
CSF	-	cerebrospinal fluid
CT	-	computed tomography
ECT	-	emission computed tomography
EM	-	expectation maximisation
FBP	-	filtered backprojection
[^{18}F]-FDG	-	flourine-18 fluorodeoxyglucose
FOV	-	field of view
FWHM	-	full width at half maximum
GM	-	grey matter
HBP	-	Hoffman brain phantom
LOR	-	line of response
LSO	-	Lutetium orthosilicate
LYSO	-	Yttrium activated lutetium orthosilicate
MLEM	-	maximum likelihood expectation maximisation
MRI	-	magnetic resonance imaging
NaI(Tl)	-	Thalium doped sodium iodide
NEMA/IEC	-	National Electrical Manufacturers Association/International Electrotechnical Commission
OSEM	-	ordered subset expectation maximization
PET	-	positron emission tomography
PSF	-	point spread function
RAMLA	-	row action maximum likelihood algorithm
SNR	-	signal to noise ratio
SUV	-	standardised uptake value
TOF	-	time of flight
VOI	-	volume of interest
WM	-	white matter

Chapter 1: Introduction

Positron emission tomography (PET) is a nuclear medicine functional imaging modality used for measuring the uptake of radioactivity, e.g. [^{18}F] fluorodeoxyglucose (FDG) in the body of the patient, amongst others in the brain. Modern reconstruction techniques have been developed and optimised for whole body imaging. Similar optimisation has not been implemented for brain imaging. This research was instituted to optimise brain reconstruction techniques.

1.1 Background: Physics of PET

1.1.1. Introduction

After intravenous administration of [^{18}F]-FDG, it is taken up according to the normal biodistribution of FDG. ^{18}F decays by positron emission, therefore the positron undergoes annihilation by combining with an electron with the production of two annihilation photons of 511 keV travelling in opposite directions. The photons emitted from the organ of uptake are detected by a PET camera equipped with the electronics to allow the simultaneous recording of the two opposing photons. The line connecting the opposing detectors is called the line of response (LOR), along which the point of annihilation will fall. The detailed function of the PET camera will be discussed below.

1.1.2. Radionuclides

Positron emitters do not normally exist in nature. They are artificially produced using cyclotrons. This process involves the acceleration of charged particles (e.g. protons and alpha particles) to high energies. These high-energy particles are then used to bombard stable target elements to produce unstable proton-rich radioactive isotopes which decay by either electron capture or positron emission (Turkington, 2001; Spinks, 2000). Positron emitting radionuclides attain stability by undergoing radioactive decay with the emission of a positron (e^+) and a neutrino (υ) (equation 1).

$$ {}^{A}_{Z}X_N \rightarrow {}_{Z-1}{}^{A}Y_{N+1} + e^+ + \upsilon \qquad \text{equation (1)} $$

Where : A= mass number
Z= atomic number
N= neutron number
X= parent radionuclide
Y= daughter nuclide

The neutrino produced in the process is not useful for nuclear medicine imaging but causes variation in the energy of the positron as the gamma energy is shared between the positron and the neutrino. Radionuclides that are used in PET imaging include ^{11}C, ^{15}O, ^{18}F and ^{13}N, which have characteristic properties that lead to their successful application as *in vivo* radiotracers. The desirable characteristics are: i) short half-life with relatively low radiation dose to patients, and ii) isotopes of elements that make up organic molecules normally present in the body enabling their incorporation without altering biochemical behaviour when used as labels (Spinks, 2000; Surti *et al., 2004*). Table 1.1 lists the positron energies of positron emitters commonly used in PET imaging and their range in soft tissue.

Table 1.1: Positron ranges in soft tissue for the principal positron emitters (Surti et al., 2004)

Positron emitter	Half life (min)	Positron energy (MeV)		Positron range in soft tissue (mm)	
		Maximum	Mean	Maximum	Mean
^{18}F	109.8	0.635	0.250	2.6	0.61
^{68}Ga	67.7	1.900	0.820	9.0	2.90
^{11}C	20.3	0.970	0.386	4.2	1.23
^{13}N	9.97	1.200	0.491	5.4	1.73
^{15}O	2.07	1.740	0.735	8.4	2.97

The positron emitted from the radionuclide follows a tortuous path in the medium while undergoing similar interactions to an electron including loss of energy through ionisation and excitation of atoms. After losing nearly all of its energy by Coulomb interaction with atomic electrons, the positron will combine with an electron in an annihilation event within a defined range of approximately 1 mm (Turkington, 2001; Spinks, 2000). This results in the disappearance (annihilation) of both particles and the production of two photons of 511 keV energy travelling in opposite directions, based on the annihilation equation below:

$$e^+ + e^- \rightarrow \gamma + \gamma \qquad \text{equation (2)}$$

The back to back photon emission is a result of the law of conservation of momentum (see Figure 1.1). However, the 180 degree angle between the photons' directions will only be achieved if during annihilation the net momentum of the two particles is zero. In practice, a small amount of momentum of the electron-positron pair can lead to ± 0.3 degrees of angular spread, which together with the positron range determine the physical limits of spatial resolution for PET (Spinks, 2000; Surti *et al.,* 2004).

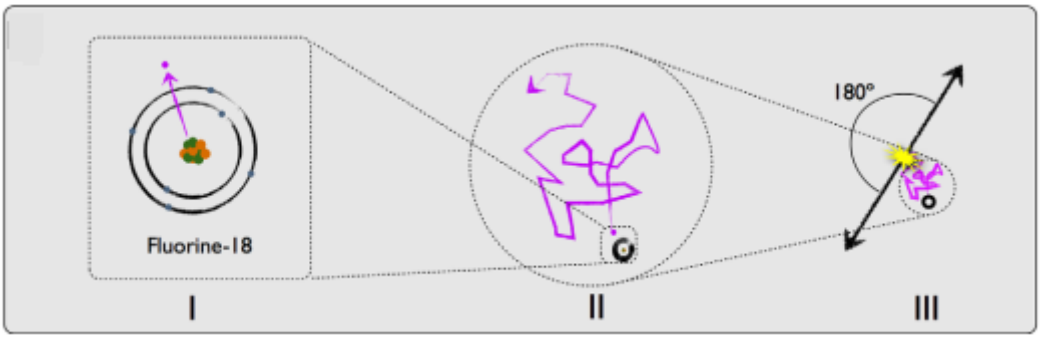

Figure 1.1: Physics of positron decay and annihilation. I) After travelling a short distance, II) the positron annihilates with the electron, III) resulting in two annihilation photons along a straight line of response (LOR) (Lonsdale and Beyer, 2010)

The two opposing annihilation photons are detected in coincidence by detectors around the patient.

1.1.3. PET Detector

A PET system commonly consists of scintillation crystals that are coupled to photomultiplier tubes. The choice of radiation detectors to use in PET systems is based on several physical characteristics and properties of the detectors, which include a) photon stopping power (efficiency), b) output signal strength, c) energy resolution, d) signal response (decay) time for high count rate applications, e) timing characteristics for time of flight (TOF), f) coincidence timing characteristics, g) ruggedness and h) hygroscopicity.

Early detector materials in PET have been sodium iodide (NaI) infused with an impurity of thallium (Tl) and bismuth germinate ($Bi_4Ge_3O_{12}$ or BGO). NaI(Tl) has a high light output and for this reason has been a detector of choice in radionuclide imaging. However, its low sensitivity and poor stopping power for 511 keV photons led to the development of BGO in search of a replacement for NaI(Tl). BGO has high stopping power and increased sensitivity for 511 keV photons, but it has poor energy resolution because of its low light output compared to NaI(Tl). PET scanners with NaI(Tl) or BGO detectors also have long scanner dead times because of their long scintillator signal

decay time (Saha, 2010; Surti *et al.,* 2004). These shortfalls led to the replacement of older generation PET scintillators with cerium doped lutetium oxyorthosilicate (LSO) because of its high light output, high stopping power and short scintillation decay time (Saha, 2010). The short scintillation decay time of LSO has reduced the coincidence window from 12 ns, typical for BGO scanners, to 6 ns and later 4 ns with development of faster electronics (Conti, 2009). Recently yttrium activated lutetium orthosilicate (LYSO) detectors that have the same properties as the LSO have also been developed and used in time of flight (TOF) PET scanners. See Table 1.2 for the characteristics of PET scintillators.

Table1.2: Characteristics of some scintillation detectors used in PET (Spinks, 2000; Saha, 2010)

Property	Thalium doped sodium iodide (NaI(Tl))	Bismuth germanate (BGO)	Lutetium orthosilicate (LSO)	Yttrium activated lutetium orthosilicate (LYSO)
Density ($g.cm^{-3}$)	3.7	7.1	7.4	7.2
Effective atomic number	51	75	66	65
Scintillation efficiency (% of NaI(Tl)	100	15	75	80-85
Scintillation decay time (ns.)	230	300	40	50
Hygroscopic	Yes	No	No	No

A dedicated PET system is designed with a ring of detectors arranged around the patient. The geometry of the block detectors can be configured in different ways depending on the scintillation detector used. Examples of typical detectors are represented in Figure 1.2.

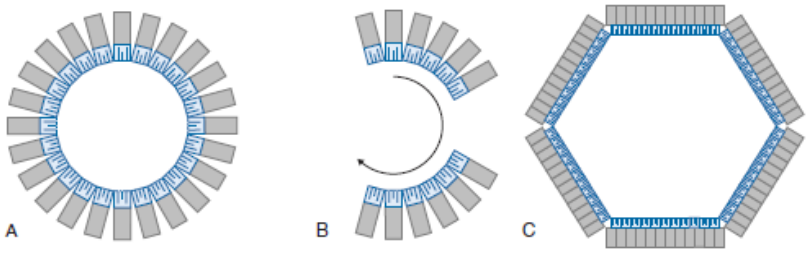

Figure 1.2: A) Full ring; B) Partial ring of detector blocks that rotates; C) Hexagonal ring (Cherry, Sorenson and Phelps, 2012)

1.1.4. PET Detection

Annihilation coincidence detection

PET is based on the detection of two 511 keV photons in coincidence by two opposing scintillation crystals that convert the photon energy into scintillation photons, which in turn will yield an electronic signal (Surti *et al.,* 2004; Saha, 2010). Simultaneous pulses from two opposing detectors is an indication that the annihilation has occurred somewhere along the path between the two detectors. This path between the two detectors is referred to as a line of response (LOR), and the simultaneous detection of two photons is referred to as coincidence (Turkington, 2001). Not all annihilation photons can be detected as some might not be detected within the coincidence window setting and will, therefore, be rejected. The rate of events processed by each detector is referred to as the single event rate for that detector.

The prompt coincidence event rate is the rate of events simultaneously detected by two detectors. Figure 1.3 depicts the event rates from two detectors in a detector ring system (Lewellen and Karp, 2004). The types of prompt coincidence events may include true events, scattered events and random events.

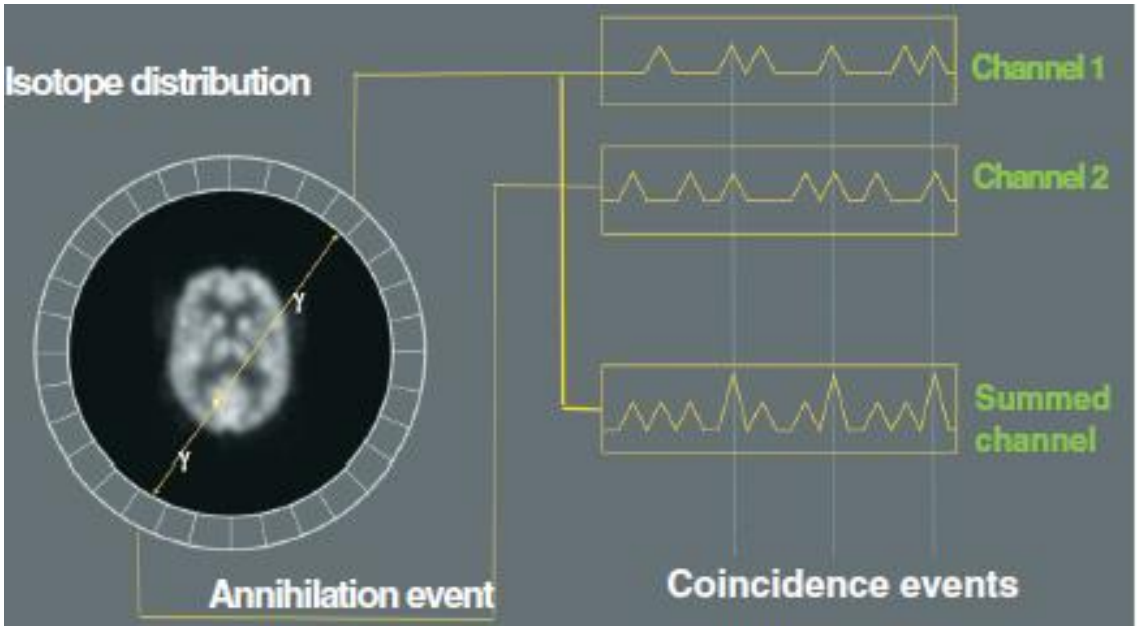

Figure 1.3: Basic PET scanner with illustration of events in coincidence (Lewellen and Karp, 2004)

True coincidence

These events occur when two 511 keV photons are produced by a single positron decay and detected without undergoing any interaction in the patient's body (Figure

1.4a). This is known as a true coincidence representing the true signal coming from the imaging object (Lewellen and Karp, 2004).

Scattered coincidence

This occurs when either one or two photons undergo Compton scatter with an atomic electron inside the body of the patient. Many of these scattering photons can still fall within the energy window and because they originate from the same annihilation, can still be detected by a detector pair within the coincidence window (Saha, 2010) (Figure 1.4b). Scattered coincidences are a contributing factor to increased image background and decreased contrast.

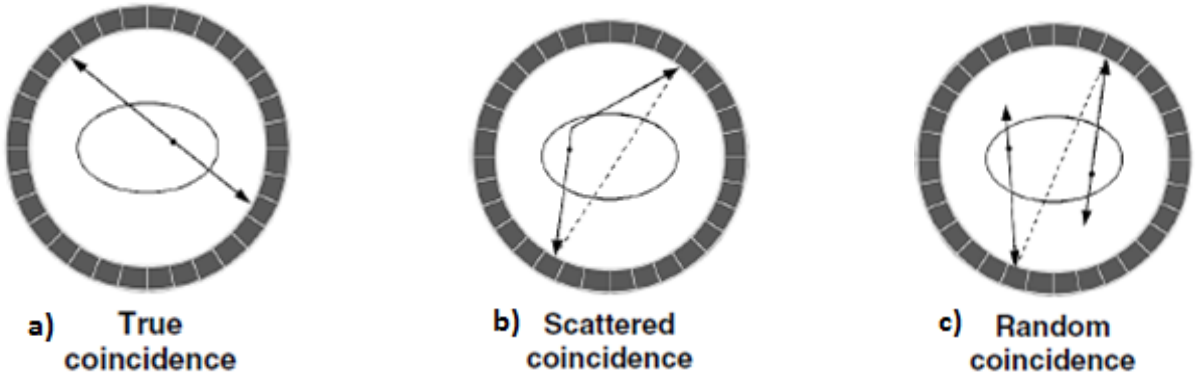

Figure 1.4: a) True coincidence; b) Scattered coincidence; c) Random or accidental coincidence (Lewellen and Karp, 2004)

Random or accidental coincidence

Random events occur when two unrelated 511 keV photons from two separate positron annihilations are detected by a detector pair within the coincidence window (Saha, 2010) (Figure 1.4c). The amount of accidental coincidence increases with a higher single event rate.

1.1.5. Theory of TOF PET

The idea of time of flight applies the use of time information when each photon is detected and the time difference between their detection. The information is used to estimate the position of annihilation along the LOR. Conventional PET systems only determine if two photons are detected within a time window of approximately 5-10 nanoseconds to verify if they belong to the same coincidence pair. When the two photons are detected within the timing window then the LOR will be formed by

activating all the voxels along the line without estimating the point of annihilation. (Conti, 2009) (Figure 1.5A).

The benefit of using TOF PET was first recorded in the early 1980's with the first generation TOF PET. However, due to the poor spatial resolution and sensitivity of the caesium fluoride (CsF) and barium fluoride (BaF_2) scintillation detectors, the first generation TOF PET systems was never used beyond the research environment (Conti, 2009).

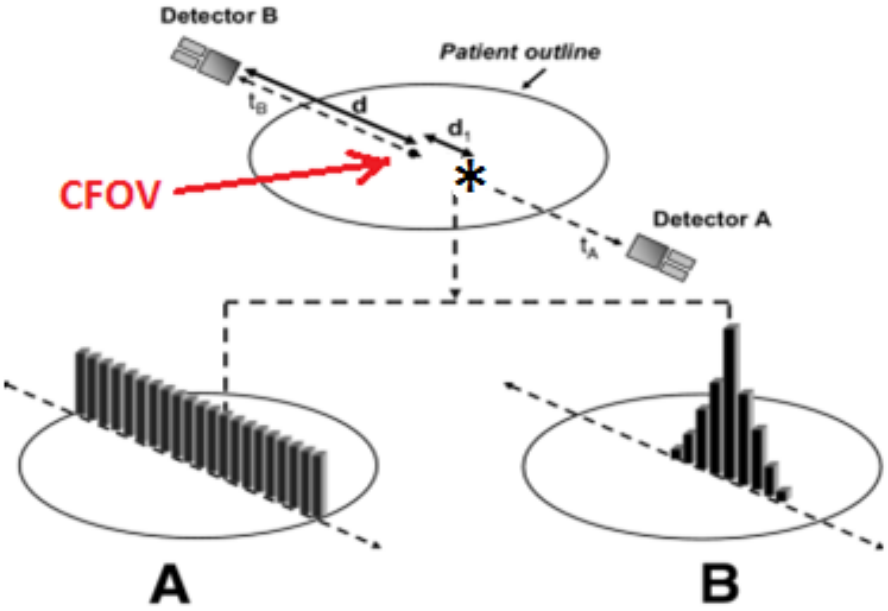

Figure 1.5: (A) Without TOF information, the annihilation is located with equal probability along the LOR; (B) Using TOF information; the annihilation point can be localised to a limited range (Townsend, 2008)

In modern PET systems TOF information helps to predict the location of the annihilation along the LOR between the two detectors (Conti, 2011). This is illustrated in Figure 1.5. Suppose the detectors are equidistant from the centre of the field of view (CFOV) with distance (d), and the positron is annihilated in the patient body at position (*) at a distance where $\Delta d = d_1$ from the CFOV. The two photons travelling to the detectors during annihilation will travel the distance $d-\Delta d$ and $d+\Delta d$ respectively. Since the photons are travelling at the speed of light (c), the time difference $\Delta t = t_A - t_B$ of arrival of the two photons at the detectors A and B can be calculated using equation 3. The location of the positron annihilation along the LOR can be estimated by measuring the time difference between the detection of the two annihilation photons. The accuracy of this estimate will depend on the PET system's precision. This is demonstrated in Figure

1.5B, in contrast to 1.5A where all the voxels within the LOR are activated (Townsend, 2008).

$$\Delta t = 2\Delta d/c \qquad \text{(equation 3)}$$

1.1.6. PET Spatial Resolution

The ability of the scanner to discriminate between two closely placed radioactive point sources determines the system's spatial resolution. Two point sources closer than the spatial resolution will appear as one, and poor spatial resolution results in decreased image contrast and inaccurate quantitation of small lesions (Daube-Witherspoon, Zubal and Karp, 2003; Tarantola, Zito and Gerundini, 2003). The method for measuring the spatial resolution of a detector system is by stimulating the detector system with a single point input and observing how it responds (Bushberg *et al*., 2002). The coincidence detector pair resolution is normally specified as a full width at half maximum (FWHM) of the point spread function (PSF) from the convolution of two individual detectors' PSF's (Lewellen and Karp, 2004). The PSF is a reflection of the widened LOR that occurs particularly near the edge of the field of view (FOV), especially with longer scintillation crystals (Mittra and Quon, 2009). The PSF describes the blurring properties of an imaging system (Bushberg *et al*., 2002).

The PSF is narrow for sources near the scanner axis but is wider for sources further from the scanner CFOV, due to the oblique penetration of the detector by the annihilation photons (Lewellen and Karp, 2004; Townsend, 2008). Figure 1.6 shows that the PSF of events near the central axis (*) is narrower than for events that occur farther away from the central axis (#). A wider PSF results in poor spatial resolution. There are three factors which limit the spatial resolution of PET scanners; i) the intrinsic spatial resolution of the detectors; ii) the average range of the positrons before annihilation and iii) the fact that the annihilation photons are not moving in exactly opposite directions to each other (Bushberg *et al*., 2002).

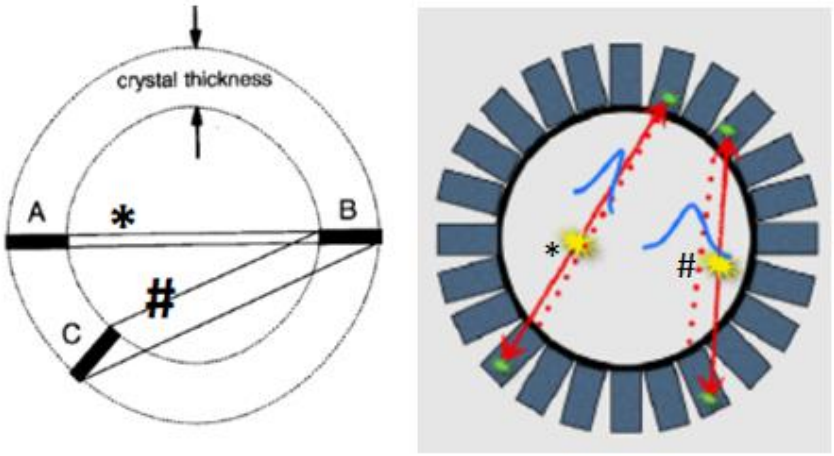

Figure 1.6: Coincidence interaction between A and B (*) results in little uncertainty in the LOR; Coincidence interaction between B and C (#) results in greater uncertainty in the LOR, which can be overcome by reducing the detector thickness which would also cause reduced detection efficiency (Bushberg et al., 2002; Lonsdale and Beyer, 2010)

1.1.7. Image Reconstruction

During imaging, after the collection of the raw data, it must be reconstructed to form an image to be used for diagnostic purposes. Two reconstruction methods are commonly used, i.e. initially filtered backprojection (FBP) and later iterative reconstruction (Mittra and Quon, 2009). The most popular of the iterative reconstruction algorithms are the maximum likelihood (ML) and the ordered subset expectation maximisation (OSEM) methods. The ML and OSEM have gained favour over FBP due to reduced streak artefacts, better signal to noise ratio in regions of low counts, and the ability to directly incorporate attenuation, scatter and resolution corrections, thereby producing higher quality images (Basu *et al*., 2011; Mittra and Quon, 2009).

An emission tomography problem can be formulated as an estimation problem where the distribution of the radiotracer inside the object has to be determined, given:

- a set of projection measurements,
- information about the imaging system used for measurement,
- a statistical description of the data, and
- a statistical description of the object.

The purpose of emission computed tomography is to obtain an image of the radioactivity distribution in the patient, thereby providing a true reflection of physiological and pathophysiological information (Vandenberghe *et al*., 2001). Reconstruction of a two-dimensional (2D) image from a series of one-dimensional (1D) projections is required for CT, SPECT and PET. A number of samples of 1D projections

p_1, p_2, p_3 . . ., p_n are acquired by a stationary system consisting of a ring of detectors. Depending on the imaging modality, the reconstructed images correspond to Hounsfield units in CT, and in SPECT and PET the reconstructed images represent the biodistribution of the injected radioactive agent (Smith and Webb, 2011). Generally, the detector is at an angle of φ degrees to the x-axis for a particular measurement, with φ having values between 0 and 360 degrees. The measured projection at every angle can be represented as $p(r,\varphi)$, where $p(r,\varphi)$ is defined as the number of scintillations detected at any location r along the detector when the detector head is at an angular position φ, and f(x,y) is defined as the estimated number of photons or positrons emitted at any point (x,y) (Figure 1.7).

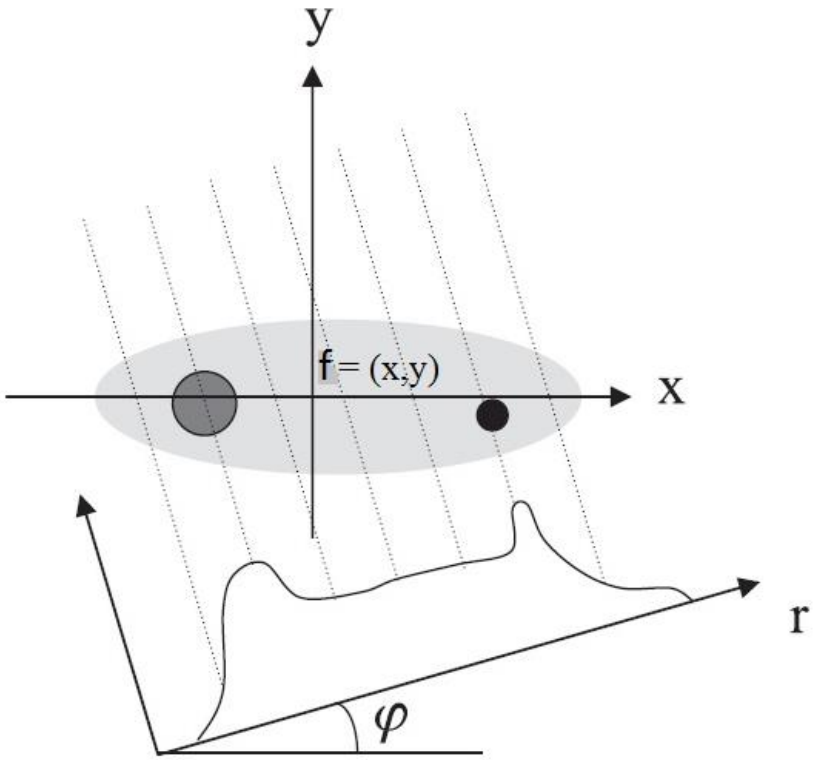

Figure 1.7: Principle of tomographic acquisition (Smith and Webb, 2011)

In SPECT, the gamma camera rotates around the patient and with the use of mechanical collimation the perpendicular incident photons are detected and produce a 2D planar image of activity distribution in the body of the patient. In PET, a detector ring is used to detect directly opposing photons from annihilations which are recorded by the electronic coincidence circuit (Vandenberghe *et al*., 2001). The 2D projections p(x,z|φ) in SPECT (all planar 2D images covering the whole circle (φ = 360°)) are rebinned into n_z (n_z = number of axial slices in z direction) 2D sinograms p(r,φ|z). Only the n_z "z-slices" creates a 3D image dataset after 2D image reconstruction.

SPECT algorithms like Siemens Flash-3D, GE Evolution or Philips® Astonish do not handle 2D sinogram slices. These resolution recovery algorithms use a special collimator model and directly reconstruct 3D images. In PET, the data acquired for each LOR are stored during data acquisition and then formatted into sinograms, where each sinogram represents one image slice. Raw data from PET can be stored as fully 3D LOR list mode data (Philips®) or as 3D sinograms (Siemens). In the latter, the LORs are rebinned into 3D sinograms with spawn and ring differences during acquisition. Explaining the image reconstruction in the 2D case simplifies the mathematical problem and allows one to figure out the main idea of the method. In simple terms a sinogram is a 2D image that uses r as column co-ordinate and φ as the row co-ordinate. In the sinogram, the horizontal axis represents the count location on the detector while the vertical axis corresponds to the angular position of the detector (see Figure 1.8) (Henkin *et al*., 2006).

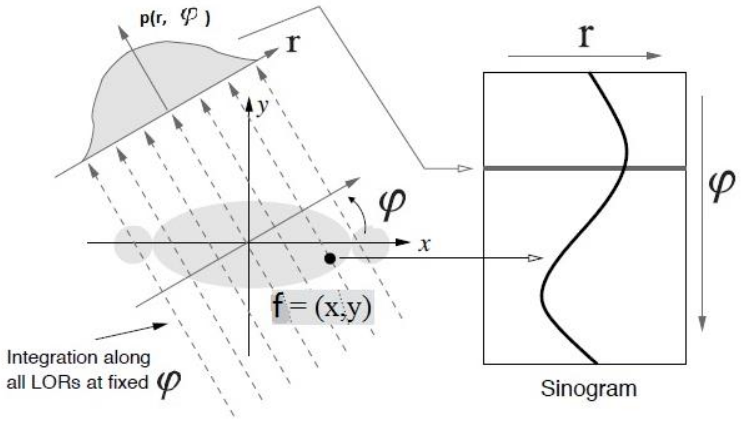

Figure 1.8: A sinogram is a projection of a slice at a given angular position (Henkin et al., 2006)

Iterative reconstruction methods may be used instead of FBP. Iterative reconstruction algorithms are based on statistical algorithms that better suit the Poisson nature of positron emission. Iterative image reconstruction starts by calculating the initial image estimate of the activity distribution in the source assuming all pixels have the same value. The forward projection step computes projections from the estimated image, and assembles them into a sinogram. The computed sinogram is then compared with the actual acquired sinogram and the difference between the two is calculated as a cost function (Figure 1.9) (Smith and Webb, 2011).

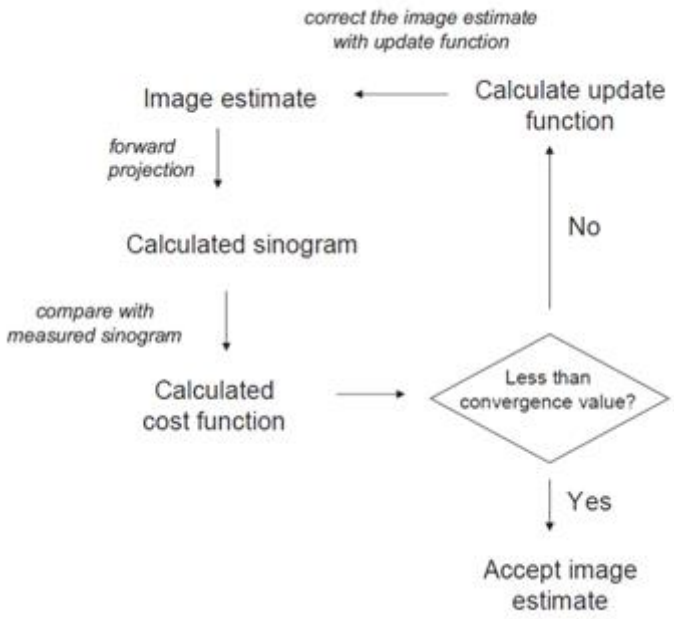

Figure 1.9: Iterative algorithm (Smith and Webb, 2011)

The cost function can be a simple sum of squares of the difference between the actual and the predicted data on the basis of each pixel. The estimated data is then updated based on the cost function to improve the similarity between the actual and the estimated data. Iterations are continued until an acceptable agreement between the input and the output is achieved (Saha, 2010).

The most widely used iterative algorithms are maximum-likelihood expectation maximisation (MLEM) and ordered-subset expectation maximisation (OSEM). Advantages of MLEM over FBP are that it: (1) does not require equally spaced projection data; (2) can use an incomplete set of projection data; (3) yields fewer artefacts and (4) allows building in more accurate models of the different physical processes involved during the measurement. The main limitations of the MLEM reconstruction algorithm are its slow convergence rate and the high computational cost of its practical implementation (Chuang *et al*., 2005). Convergence rate is the speed at which an image reconstruction algorithm achieves an image of acceptable quality. In order to counteract the computation time required for MLEM, the OSEM algorithm was developed. The OSEM method is a modification of the MLEM in which the angular projections are grouped into subsets, and MLEM is performed on each subset instead of on each projection. Suppose in an acquisition of 32 equally spaced projections around the object, the projections are grouped into 8 subsets, then each subset will contain 4 projections (Saha, 2010).

Herman and Meyer (1993) investigated and proposed the use of an algebraic reconstruction technique (ART) in a study in which they reported significantly better image quality with few iterations of ART compared to many iterations of expectation maximisation (EM). ART proved to have increased speed and significantly lower computational cost over EM. This resulted in the row action maximum likelihood algorithm (RAMLA) which can also be regarded as a faster alternative to the EM algorithm (Herman and Meyer, 1993; Browne and De Pierro, 1996). With RAMLA, the reconstructed image is updated after each projection line and the projection lines are selected in an orderly manner to ensure that sequential projection lines are as orthogonal as possible to speed up the rate of convergence (Daube-Witherspoon *et al*., 2001). In addition, 3D spherically-symmetric basis functions, or blobs, are used during image reconstruction instead of cubic voxels. They have an additional parameter that controls the shape of the blob and, subsequently, the characteristics of the images produced by the iterative reconstruction method. The additional parameter is the radius of the blob whose variation alters the volume of the blob element. Implementation of the blob volume element over the voxel element in the iterative reconstruction methods has led to substantial improvement in the reconstruction performance, based on visual quality and on quantitative measures (Matej and Lewitt, 1996). Recently, there has been an implementation of the LOR RAMLA algorithm on the Gemini scanner (Philips Medical Systems™, Cleveland, Ohio, USA) with an integrated geometric correction. A pre-processing step where raw LOR data is interpolated to evenly spaced sinogram data is used in a conventional PET image reconstruction. The LOR based reconstruction eliminates this interpolation step resulting in a better spatial resolution and image quality. In the Philips® PET/CT product, this approach is combined with a blob basis function leading to resolution preservation and significant suppression of image noise. Figure 1.10 demonstrates the difference between a voxel grid and a blob grid.

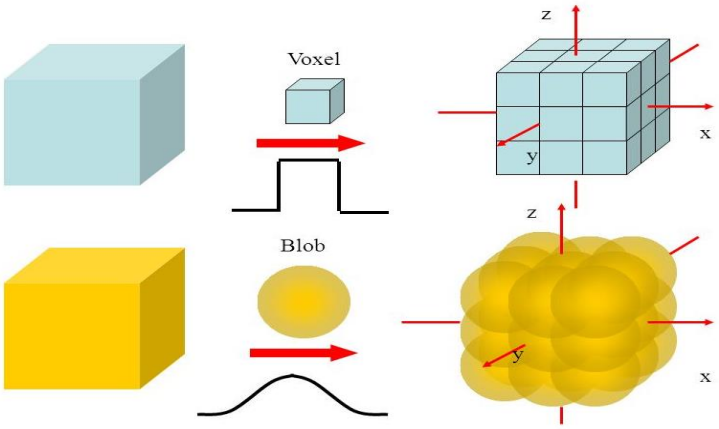

Figure 1.10: Voxel grid vs blob grid (Zeng. L., Nuyts, J. and De Man, B., 2007)

A RAMLA with system modelling of attenuation, random and scatter correction is used for the reconstruction as shown below:

$$f_i^{k,m} = f_i^{k,m-1}\left[1 + \lambda \sum_{j \in subset\ m} a_j H_{ji} \left(\frac{{}^{d_j}/_{\eta_j^{multi}}}{\sum_{n=0}^{N-1} a_j H_{jn} f_n^{k,m-1} + b_j^{add}} \right)\right]$$

Here, f_i is the image basis value element (blob) i of the emission object, j indexes the LOR in subset m, k is the iteration number, n indexes the blobs intersecting the LORs, λ is the relaxation parameter, a_j is the attenuation correction factor for LOR j, H_{jn} is the geometric system matrix element for LOR j and blob n, d_j is the data counts in LOR j, η_j^{multi} is the multiplicative correction factor for LOR j including normalisation, decay and dead time, b_j^{add} is the additive correction factor including random and scatter correction (Hu *et al*., 2007). In RAMLA, the update is controlled by the relaxation parameter λ.

With the recent advances in response, high light output and high stopping power scintillators, TOF PET is commercially available for clinical use. The Philips® Gemini TF scanner can acquire data in either LOR sinogram or in list mode format, and can reconstruct data with either TOF of nonTOF algorithms.

Figure 1.11 displays the Gemini time-of-flight PET list mode reconstruction flow chart.

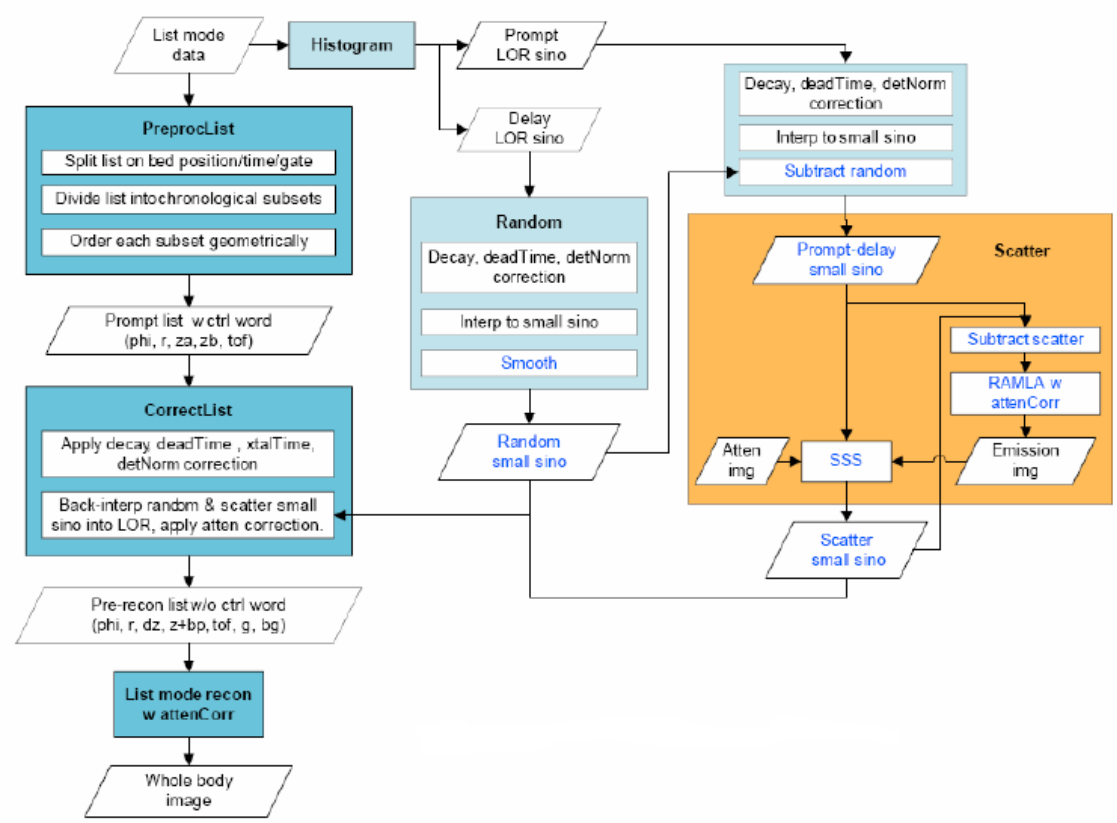

Figure 1.11: Gemini-TF PET list mode reconstruction flow chart (Wang et al., 2006)

LOR-RAMLA was developed to increase the convergence rate of image reconstruction by incorporating the Poisson nature of sinogram and using cyclic projection permutation. LOR-RAMLA is the current default reconstruction of the Gemini TF scanner in brain mode. The maximisation of the cost function differs (row action and relaxed ordered subsets expectation maximisation). The relaxed BLOB OS (spherically symmetric basis function ordered subset algorithm) is the newer reconstruction mainly developed for whole body imaging on the Gemini system with the implementation of time of flight which is not available with LOR RAMLA.

On one side there is a practical reason to compare the three algorithms (availability on the system), while on the other side there are different iterative approaches (RAMLA/OSEM) which should have different behaviours in convergence, noise and contrast.

The aim of the study was to investigate the effect of different image reconstruction parameters on PET/CT images with the objective of evaluating these algorithms for quantification of FDG PET brain imaging.

1.2. Literature Review

1.2.1. Introduction

The literature review was performed using PubMed as a search engine, focusing on specific journals and relevant books in the Stellenbosch University library. The specific journals were Journal of Nuclear Medicine, Molecular Imaging and Biology, IEEE Transactions on Medical Imaging, Nuclear Medicine Communications, Journal of Nuclear Medicine Technology, Physics in Medicine and Biology, and European Journal of Nuclear Medicine and Molecular Imaging. The keywords used were TOF, PSF, PET/CT, Brain, and LOR RAMLA. The literature cited was from 1993 onwards.

1.2.2. Use of TOF PET imaging

Karp *et al.* (2008) investigated the benefit of time of flight (TOF) in PET imaging using a Philips® Gemini TF PET/CT scanner. Images of 27 and 35 cm diameter cylindrical phantoms were acquired. In each phantom were spheres varying in size from 10 to 37 mm in diameter, with each sphere filled with different concentrations of activity. Reconstruction was performed using maximum likelihood expectation maximisation (MLEM) with and without TOF. They varied scan duration from 1 min to 5 min, and the number of iterations from 1, 2, 5, 10 and 20 using 33 subsets. It was found that TOF led to improved contrast and faster convergence compared to nonTOF. These results have not been tested on small object imaging, e.g. that of the brain. In addition, this study did not explore the effect of increasing scan duration beyond 5 min or iterations beyond 20.

Taniguchi *et al.* (2015) also investigated the effect of TOF as well as PSF on improving PET/CT image quality. This group used a National Electrical Manufacturers Association/International Electrotechnical Commission (NEMA/IEC) body phantom, and a 40 cm diameter large phantom, resembling a patient with a larger body size. Different combinations of reconstruction algorithms were used, namely baseline OSEM, OSEM+PSF, OSEM+TOF and OSEM+PSF+TOF. Noise and contrast were assessed in relation to phantom size, radioactivity, acquisition time and number of iterations. Acquisition time was varied from 1-10 min and iterations from 1 to 10. Twenty-four subsets were used for algorithms without TOF and 21 subsets for the TOF algorithms. PET/CT image quality showed improvement when TOF and point spread function (PSF) information were included in the reconstruction. The same group further assessed image quality by visual inspection, coefficient of variation in the NEMA

phantom, signal to noise ratio (SNR) and contrast of a 10 mm sphere (Akamatsu *et al*., 2012). They demonstrated the highest SNR for OSEM+PSF+TOF and suggested a necessity to optimise reconstruction parameters for the best results when using TOF or PSF. These studies, similar to Karp *et al.* (2008), did not evaluate the effect of longer acquisition times above 10 min, and larger number of iterations above 10, on image quality. In addition, the effect of varying imaging parameters on smaller objects such as brain was not evaluated.

Suljic *et al.* (2015) explored the influence of various TOF and nonTOF reconstruction algorithms on PET/CT image quality. Measurements were made on the triple line and Jasczack phantoms with incorporation of PSF in filtered back-projection (FBP), OSEM and iterative reconstruction. Reconstructions were also performed with and without TOF. The added TOF information reduced background variability while improvement of spatial resolution was found to be negligible.

Wilson and Turkington (2013) conducted a study where the improvement of image quality with TOF versus nonTOF PET was parameterised by measuring the SNR of 1 cm spheres in a range of body sizes. Results showed that there were no image quality improvement between TOF and nonTOF for a patient diameter less than 17.5 cm. This study suggested that the addition of TOF information will not lead to an improvement in image quality for small objects.

Kadrmas *et al.* (2009) evaluated the effect of TOF for detecting and localising focal hot lesions in noisy PET images. In this study, an anthropomorphic lesion detection phantom to mimic whole body oncologic [^{18}F]-FDG PET with a number of spherical lesions of diameters 6 to 16 mm distributed throughout the body, was scanned on a TOF PET scanner. The data was reconstructed with the standard LOR-OSEM, with the inclusion of both PSF (LOR-OSEM+PSF) and TOF (LOR-OSEM+TOF). The lesion detection performance of each reconstruction was compared and ranked, using localisation receiver operating characteristic analysis by both human and numeric observers. It showed that TOF PET provided a significant improvement in observer performance for detecting focal hot lesions in a noisy background. The same group investigated the effect of scan times on oncologic lesion detection in whole body PET imaging and found that the images reconstructed using TOF information with 40% shorter acquisitions provided equivalent lesion detection performance to scanning

without TOF information (Kadrmas *et al*., 2012). It would be of value to determine if the same is applicable to brain imaging.

LOR RAMLA is regarded as a faster algorithm than the expectation maximisation (EM) algorithm according to Browne and De Pierro, (1996). Fewer iterations of RAMLA were needed to achieve comparable results to more iterations of the EM algorithm. The EM algorithm could be accelerated using chronological ordered subsets on line of responses (Popescu, Matej and Lewitt, 2004). Wang *et al.* (2006) have shown that TOF information can be incorporated as a TOF kernel width on BLOB OS algorithm. This TOF reconstruction converged faster and had better contrast to noise trade-offs than nonTOF reconstruction.

Akamatsu *et al.* (2014) investigated the effects of PSF and TOF on the standardised uptake value (SUV) of lymph node metastases with [^{18}F]-FDG PET/CT. The PET data was reconstructed with the standard OSEM algorithm, OSEM+PSF, OSEM+TOF and OSEM+PSF+TOF. A semi-quantitative analysis using maximum and mean SUV of lymph node metastases and mean SUV of normal lung tissue was done. It was found that using PSF and TOF information both increased the SUV of the metastatic lymph nodes, and improved small-lesion detectability. The study suggested that caution must be exercised since PSF and TOF can affect the accuracy of quantitative measurements.

Another parameter which can influence contrast and noise is the relaxation parameter lambda (λ). Applying lower λ values creates a broader PSF, and therefore smoother images. Groheux *et al.* (2009) tested the impact of different values of λ on contrast and noise when using the line-of-response row-action maximum likelihood algorithm (LOR-RAMLA) in [^{18}F]-FDG PET/CT. A NEMA/IEC torso phantom was used to acquire the data on a Philips® Gemini GXL PET/CT scanner. The data were reconstructed with λ values ranging from 0.025-0.1, and the quality of the reconstructed images was evaluated by contrast recovery coefficient and background variability values. In this study, it was found that the contrast recovery coefficient and background variability increased significantly when λ was increased. The use of a large relaxation parameter increased the convergence with the trade-off of increasing noise.

1.2.3. Use of TOF PET in brain imaging

Leemans *et al.* (2015) investigated the blob based reconstruction characteristics using different parameters for optimisation of brain image quality in PET/MRI. Two sets of phantoms were used: the Hoffman brain phantom and the NEMA 2007 image quality phantom. All sets of images were reconstructed using a list mode TOF OSEM algorithm as well as a blob based reconstruction. It was concluded that optimised blob parameters improved the quality of reconstructed images, however, this improvement could be task specific depending on the desired image characteristics extracted. However, the investigation was only limited to PET/MRI.

Zeimpekis *et al.* (2015) compared the perfomance of the PET components between TOF PET/CT and TOF PET/MRI, using brain and whole body images from both PET/CT and PET/MRI. The images were compared for image quality, image sharpness, artefacts and noise. In conclusion, TOF PET/MRI showed higher image quality compared to TOF PET/CT, mainly for body imaging with no significant difference in brain images. This study did not compare different reconstruction parameters.

Nagaki, Onoguchi and Matsutomo (2014) investigated the effect of changing counting rates on the image quality of brain FDG PET/CT studies. Combinations of the Gaussian filter (GF), point spread function (PSF) and the TOF were studied on the images obtained with different counting rates. Quantitative analysis of the brain cortex image quality was made by evaluating spatial resolution, contrast, and signal-to-noise ratio. It was found that applying the GF improved SNR but reduced contrast and spatial resolution, whereas PSF and TOF improved the SNR, contrast and spatial resolution. However, this study did not look at different numbers of iteration.

A study by Prieto *et al.* (2015) assessed the influence of different algorithms on PET image quality of brain phantoms. A HBP was imaged on a PET/CT system that had capability of applying TOF and PSF parameters. Iterative reconstruction was used for image processing, with 4 models applied to the data, namely OSEM, OSEM+TOF, OSEM+PSF and OSEM+PSF+TOF. It was demonstrated that increasing the number of iterations resulted in an increase in contrast while increasing noise as well. This was consistent with the findings of Groheux *et al.* (2009). The number of iterations used in this study was only up to 10.

Most of the studies discussed above used different PET/CT scanners than the Phillips Gemini TF Big Bore scanner available at Tygerberg Academic Hospital. These scanners have different detector designs (block-detectors), sinogram-based data acquisition (rebinned LORs) and some do not use fully 3D LOR-based TOF or nonTOF reconstruction. The effect of TOF on image quality in brain imaging or imaging of smaller objects has not been discussed in depth, although some pointed out that optimisation in reconstruction algorithms is worthwhile to improve image quality.

1.3. Problem Statement

It has been proven that TOF imaging improves lesion detection and localisation, with a greater impact in larger patients (Karp *et al*., 2008; Taniguchi *et al*., 2015; Suljic *et al*., 2015; Kadrmas *et al*., 2009). As there were only a few studies focusing on small object image optimisation (Leemans *et al*., 2015; Nagaki, Onoguchi and Matsutomo, 2014; Zeimpekis *et al*., 2015), this necessitated the current investigation of the impact of TOF on smaller diameter objects such as the brain. When TOF is applied, image quality is expected to improve due to the improved ability to localise the emission events. However, improvement in image quality may only occur if the size of the object being imaged is greater than the positional uncertainty of the measurement. The effect of TOF on the limited diameter of the head or brain needed to be investigated. Currently, there is minimal published data available on this topic.

According to Tarantola, Zito and Derundini (2003), iterative algorithms are based on the attempt to maximise or minimise a target function determined by the particular algorithm used. The target is reached through several analytic processes called iterations. Different numbers of iterations are required to reach convergence, but this group suggested that too much iteration can easily lead to noise amplification with image quality deterioration. For this reason, it is important to perform an accurate evaluation of the ideal number of iterations needed to obtain the best image quality. The number of iterations represents different positions on the relaxation curve. The relaxation parameter affects the convergence, and has an influence on the update step. It is well known that the statistics of the raw data also has an influence on the convergence and especially on the variance in the reconstructed image.

Zeimpekis *et al*. (2015) perfomed a clinical evaluation of PET image quality as a function of acquisition time on a new TOF PET/MRI compared to TOF PET/CT. The

image quality investigated in this study was only that of the PET component of the two modalities, analysing the SUV as a function of acquisition time. Brain and whole body patient studies were included in this study where the PET/CT scan was used as reference. PET/CT and PET/MRI images were acquired and the acquisition times reduced to assess the performance of PET/MRI for lower count rates, image quality, image sharpness, artifacts and noise. This was compared to the PET/CT images which were used as the gold standard. For quantification, the SUV measurements in the liver and in the white matter were taken for comparison. From their findings, it was concluded that the TOF-PET/MRI showed higher image quality compared to TOF-PET/CT with reduced imaging times. However, no significant differences were found in brain imaging.

1.4. Hypothesis

- The optimisation of different image reconstruction parameters (number of iterations, lambda (λ), and scan duration) will enhance the quality of brain images on a Philips® Gemini TF Big Bore PET/CT scanner.
- The inclusion of time of flight (TOF) information in the reconstruction algorithm will enhance brain image quality on a Philips® Gemini TF Big Bore PET/CT scanner.

1.5. Aims and objectives

To investigate the effect of different image reconstruction parameters on PET/CT images with the objective of evaluating these algorithms for quantification of FDG PET brain imaging.

1.5.1. Specific objectives:

(i) to determine the optimum number of iterations needed for acceptable image quality,

(ii) to investigate the effect of different relaxation parameters (lambda value) on reconstruction algorithms,

(iii) to evaluate the effect of varying scan times on signal to noise ratio in reconstructed brain images, and

(iv) to investigate the effect of the use of time of flight (TOF) information on reconstruction algorithms.

Chapter 2: Materials and methods

This study was performed at the Western Cape Academic PET/CT Centre in the Division of Nuclear Medicine of Tygerberg Academic Hospital.

2.1. PET/CT scanner

A Gemini TF Big Bore PET/CT scanner manufactured by Phillips was used to acquire the images. The system is comprised of a PET scanner combined with a 16-slice CT scanner. It has a scanner ring diameter and patient bore diameter of 90.34 and 71.70 cm, respectively. The PET detectors are comprised of yttrium-doped lutetium oxyorthosilicate (LYSO) with dimensions of 4x4x22 mm^3. It is a fully 3D scanner with an energy resolution of 11.5% (FWHM) at 511 keV with threshold energies of 440 and 665 keV (Surti, *et al*., 2007). The system's temporal resolution measured with a low activity (approximately 3.7 MBq) point source in air is 585 ps (FWHM), 25 ps timing bin and 4.8 mm intrinsic spatial resolution which translates to a positional uncertainty of 9 cm (FWHM) along the line pair (Karp and Fletcher, 2006). The bed has a deep U-shaped head holder with a 2.54 cm thick foam insert used to fixate both patients and the brain phantom during scanning.

2.2. Phantom Data

Phantom data was acquired using a 3D Hoffman brain phantom (HBP). This phantom consists of 19 plexiglass plates stacked into a cylinder of inside diameter and height of 20.8 cm and 17.5 cm respectively, and a fillable volume of 1.2 litres. Each of 19 inserts is made up of five thinner slices on the interspace. The HBP allows for qualitative and quantitative study of 3D radioisotope distribution corresponding to a FDG PET brain study. The phantom simulates the 4:1 uptake ratio between the gray and white matter. The phantom was filled with [^{18}F]-FDG solution of approximately 40 MBq activity at time of scan. Liquid soap was added to the solution to reduce accumulation of bubbles. Once filled, the HBP was positioned in the scanner, with the central axis of the cylinder coplanar to the centre of the axial FOV. A low dose CT scan (120 kV, 90 mAs) was performed for anatomical localisation and attenuation correction, followed by an emission scan acquired in list mode for a duration of 25 min.

2.3. Ethics

This study was approved by the Health Research Ethics Committee of the Faculty of Medicine and Health Sciences of Stellenbosch University (Ref S13-01-011). Written informed consent was obtained from every patient in accordance with the 2008 Helsinki Declaration.

2.4. Patient selection

Patients referred to the Western Cape Academic PET/CT Centre to undergo whole body PET/CT for oncological imaging were selected for the study.

On the day of their clinical PET booking, patients typically reported to the PET Centre with their referral forms in order to receive advice on scan preparation. If practical, screening for study inclusion, followed by informed consent, was conducted in a private office during this visit. If it was not practical for the patient to have this discussion on the day of the booking, the patient was invited to join the study on the day of their oncology scan. The study was explained to them and questions were answered before informed consent was obtained.

If the patient consented, his/her participation did not influence the timing of the clinical study. The brain PET/CT imaging was done 30 min post injection and lasted for 25 min. Imaging was, therefore, completed 5 min before the start of the clinical whole body PET/CT scan. The radiation exposure related to CT for whole body could range from 1-20 mSv and with an additional dose of about 0.02 mSv from the low-dose CT needed for attenuation correction (Varrone *et al*., 2009). Thus patients were not exposed to a significant additional radiation dose.

Patients were selected to participate in the study according to the following criteria:

<u>Inclusion criteria</u>

1) age 18 years or older
2) able to give written informed consent
3) no neurological symptoms
4) normal neurological exam
5) English, Afrikaans and Xhosa speakers

Exclusion criteria

1) current or previous substance dependence other than nicotine and moderate alcohol usage
2) lifetime or current diagnosis of psychiatric disorder
3) recent chemotherapy
4) use of any psychotropic medication
5) medical or neurological illness or trauma that could affect the central nervous system (CNS), including brain tumour, paraneoplastic syndrome, severe renal, hepatic, pulmonary, an endocrine disease, or significant head injury
6) known abnormalities on previous brain imaging
7) pregnant women
9) fasting blood glucose >7.2 mmol/l
10) diabetes mellitus
11) pathology that makes central nervous system involvement difficult to exclude with a high degree of certainty e.g. small cell lung cancer, advanced melanoma
12) evidence of CNS pathology on PET or CT

2.5. Brain PET/CT Scanning

Preparation for the brain scan is similar to the clinical scan preparation: before the study the patient needed to confirm the appointment, and was advised to fast for 6 hours prior to the scan and to avoid intake of caffeine. They were instructed to drink plenty of water and to avoid any alcohol or drugs since these may affect cerebral glucose metabolism.

On arrival, patients were taken to the examination room where the registrar interviewed them and explained the procedure thoroughly to them. They were selected for the study if they fulfilled the screening criteria and if willing, informed consent was obtained if it was not done before.

An intravenous line was inserted and blood glucose levels checked for each patient. Participating patients were instructed not to speak, read or be otherwise active 10 min before to 20 min after FDG administration. Patients were required to sit on a

reclining chair in a quiet dimly lit cubicle with eyes open for this period. After relaxing for at least 10 min, patients received a dose of 175-350 MBq of [^{18}F]-FDG depending on their weight, according to the existing PET/CT imaging protocol.

At 20 min post injection the patient was requested to empty his/her bladder on route to a change room prior to starting imaging. To minimise movement artefacts, the patient was informed to avoid movement of the head, and the patient's head was fixated into the deep U-shaped head holder.

Brain PET/CT acquisition commenced 28 min after injection of FDG using a Philips® Gemini TF Big Bore PET/CT scanner. The low-dose CT component was performed first for 2 min followed by a 25 min PET acquisition in list mode. The low dose CT scan was used for attenuation correction with acquisition parameters of a current of 20 mAs and a tube voltage of 120 kV. Shortly after the brain PET/CT was completed, the patients' PET/CT scanning for their routine oncology management proceeded at 60 min post injection as per the standard protocol.

After the acquisition of the brain PET/CT, data quality was checked for the following before inclusion in the study:

- whole brain is in the field of view
- adequate counts are obtained (50-200 x 10^6 counts)

2.6. Image reconstruction

The PET system has a dedicated powerful computing platform for implementing fully 3D PET iterative reconstruction algorithms (LOR based list mode reconstruction). This platform uses a 5-node quad core CPU computer cluster, thereby making it possible for the image processing to proceed in parallel with data acquisition. Image processing for a typical whole body study usually takes 10 to 30 min after the end of acquisition depending on the number of counts collected. For PET/CT reconstruction, the same brain dynamic reconstruction protocol used for clinical brain imaging at the Western Cape Academic PET/CT Centre was used. This reconstructs 5 dynamic frames of 5 min each using a 3D LOR RAMLA algorithm. For a whole body PET, BLOB OS algorithm with spherically symmetric basis functions voxels representing the emission object, was used. The BLOB OS reconstruction has the ability to reconstruct images

with or without applying TOF. The CT data were applied for attenuation correction of the PET data.

The following algorithms were used to reconstruct the acquired PET images: (a) LOR RAMLA subsequently called RAMLA; (b) BLOB OS without TOF called BLOB nonTOF, and (c) BLOB OS with TOF called BLOB TOF. All the reconstructions were done with 33 subsets and with a varying number of iterations (3, 5, 10, 15, 20 and 30) and for two values of the relaxation parameter lambda (λ). The relaxation parameter lambda (λ) was varied between smooth (λ= 0.7) and normal (λ=1.0) (no relaxation), according to the default settings on the PET/CT system. To study the effect of the raw data signal-to-noise ratio on each reconstruction algorithm, subsections of the 25 min acquired data were reconstructed with a constant number of 30 iterations. The acquisition time intervals were varied as follows: 0-3, 0-5, 0-10, 0-15, 0-20 and 0-25 min.

After the reconstruction of the brain PET/CT, data quality was checked for the following before inclusion in the study:

- misregistration between the CT and the PET data
- movement during the PET acquisition

2.7. Phantom data analysis

Two CT scans with high resolution and a low pitch to obtain a very good axial sampling were performed when the 3D Hoffman brain phantom was filled with water. The two CT images were coregistered and a mean image was created. Based on this image, MRIcro (version 1.40 build 1) was used to define a number of volumes of interest (VOIs). This was done using the 3D regions of interest (ROI) tool. This tool was used to specify seed voxel (in voxel coordinates in MRIcro) difference from origin, difference at edge, radius in mm and number of erode/dilate cycles. The VOIs listed in Table 2.1 and shown in Figures 2.1 to 2.9 were defined. Seed in Table 2.1 refers to the seed voxel of the algorithm used in MRIcro to define the VOI. It is the starting voxel of a region growing algorithm based on intensities. Settings in Table 2.1 refer to the specifications of the lesion growing algorithm used in MRIcro (e.g. the maximum change in intensity). These settings are given explicitly so that the VOI is fully reproducible if a researcher would start from the same image and use the publicly available MRIcro software.

Table 2.1: Seed voxel coordinates and setting for different VOIs used

CORTICAL REGIONS	**SEED**	**SETTINGS**
R parietal	63 - 68 - 160	15/10/20/2
L parietal	142 - 64 - 160	15/10/20/2
R frontal	67 - 231 - 153	15/10/24/2
L frontal	139 - 223 - 153	15/10/24/2
R temporal	36 - 152 - 38	15/10/20/2
L temporal	182 - 160 - 38	15/10/20/2
Ant cingulate	98 - 208 - 131	15/10/15/0
SUBCORTICAL REGIONS	**SEED**	**SETTINGS**
R putamen	68 - 171 - 95	15/10/15/2
L putamen	134 - 171 - 95	15/10/15/2
R thalamus	88 - 142 - 100	15/10/15/2
L thalamus	112 - 142 - 100	15/10/15/2
R caudate nucleus	83 - 183 - 105	15/10/15/2
L caudate nucleus	117 - 179 - 105	15/10/15/2
WHITE MATTER AND CEREBROSPINAL FLUID (CSF)	**SEED**	**SETTINGS**
R WM	73 - 188 - 161	25/20/15/2
L WM	127 - 188 - 161	25/20/15/2
CSF	101 - 162 - 111	20/20/35/3

All VOIs were exported as an image in neuroimaging informatics technology initiative (nifti) format. They were then coregistered to the PET images of the HBP after confirming that all PET reconstructions were in exactly the same space before generating the mean image. This mean image was taken as the reference image. The source image was the mean CT image of the brain used to define the VOIs. Other images are all the different VOI images. Interpolation for the resliced options is set to nearest neighbour.

An iterative algorithm is said to converge when, as the iterations proceed, the output gets closer and closer to a true value. Full convergence for each algorithm in this study was taken as the convergence value where the graph reached a plateau. Convergence percentage was calculated as the ratio of grey matter to white matter (GM/WM) value at 3 iterations to the value at a different number of iterations multiplied by 100.

The geometric mean is useful when comparing data with very different properties. For **n** numbers all are multiplied and the n^{th} root (written $\sqrt[n]{}$) taken.

For example, for **n** numbers, $\mathbf{a_1}$ to $\mathbf{a_n}$, calculating the geometric mean is as follows:

$$\sqrt[n]{(a_1 \times a_2 \times \ldots \times a_n)}$$

Once the VOIs were co-registered with the PET images, the mean counts, the normalised mean counts and the coefficient of variation (COV) were calculated using a MATLAB R2013a code. The normalised mean counts were defined as the ratio of the mean counts in the VOI to the total counts in the whole brain. The COV is defined as the ratio of the standard deviation of the mean count (σ) to the mean counts (μ).

$$COV = \frac{\sigma}{\mu}$$

The COV is presented as percentage, with a low value of COV corresponding to high precision and a high value corresponding to lower precision.

Figures 2.1 to 2.9 are the transverse (A) and coronal (B) slices of the Hoffman brain phantom showing the selected VOIs that were used for the analysis.

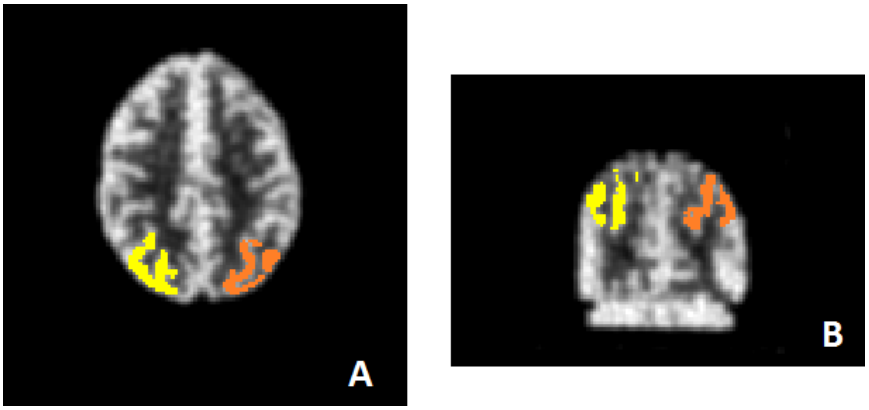

Figure 2.1: VOI for the left and right parietal cortex

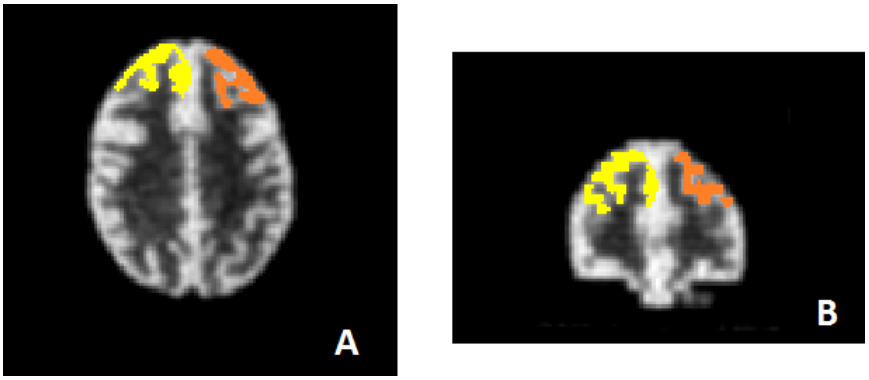

Figure 2.2: VOI for the left and right frontal cortex

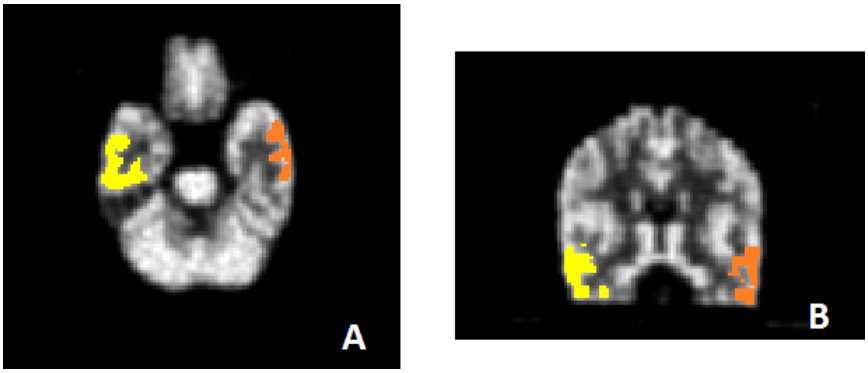

Figure 2.3: VOI for the left and right temporal cortex

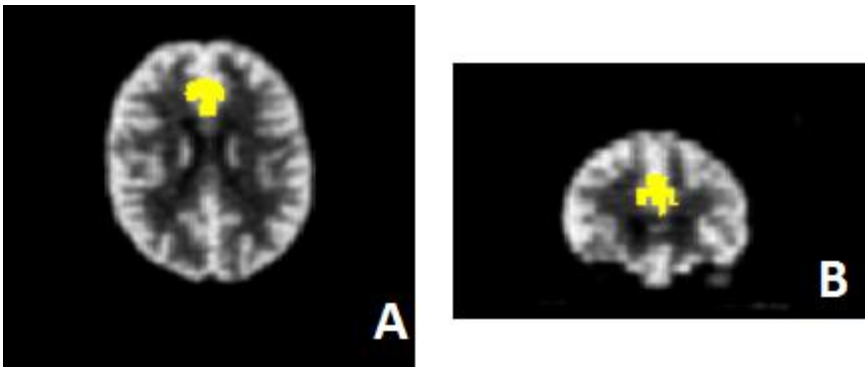

Figure 2.4: VOI for the anterior cingulate

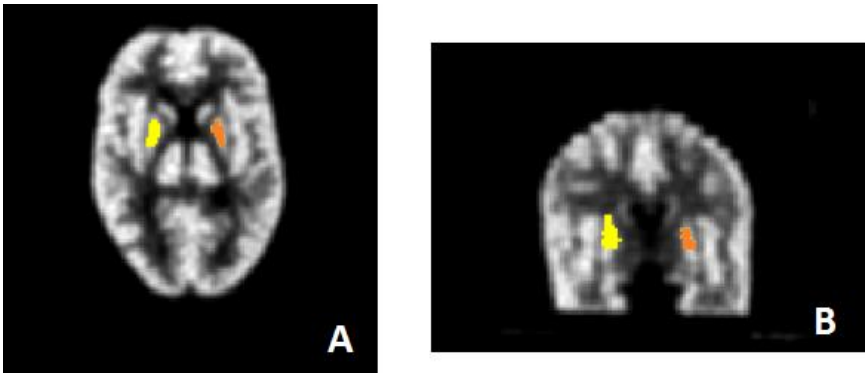

Figure 2.5: VOI for the left and right putamen

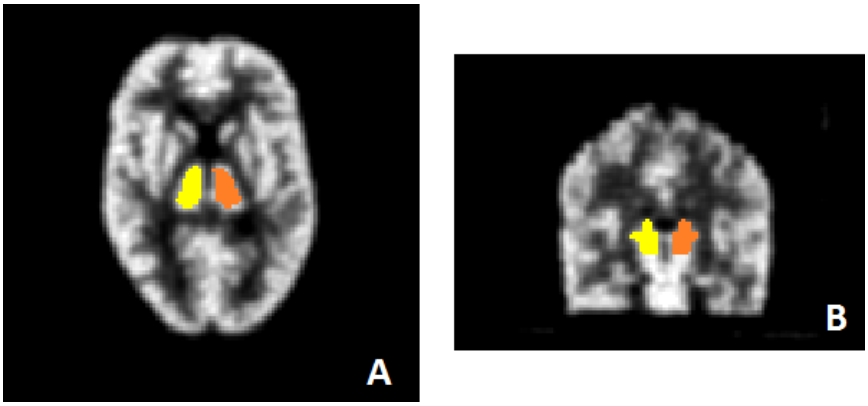

Figure 2.6: VOI for the left and right thalamus

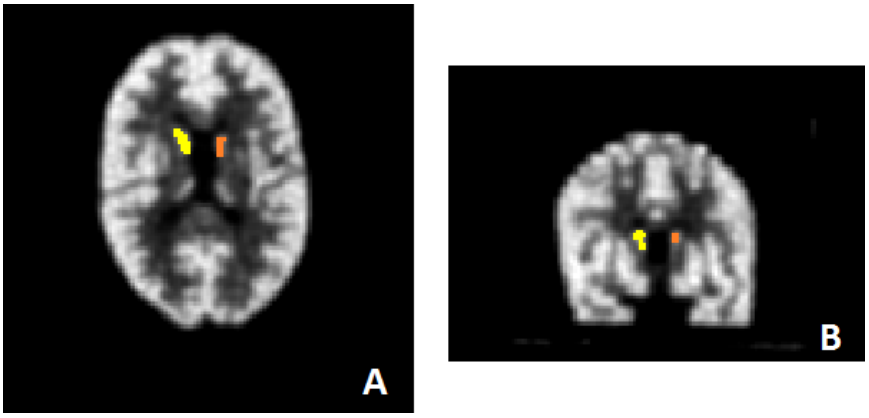

Figure 2.7: VOI for the left and right caudate nucleus

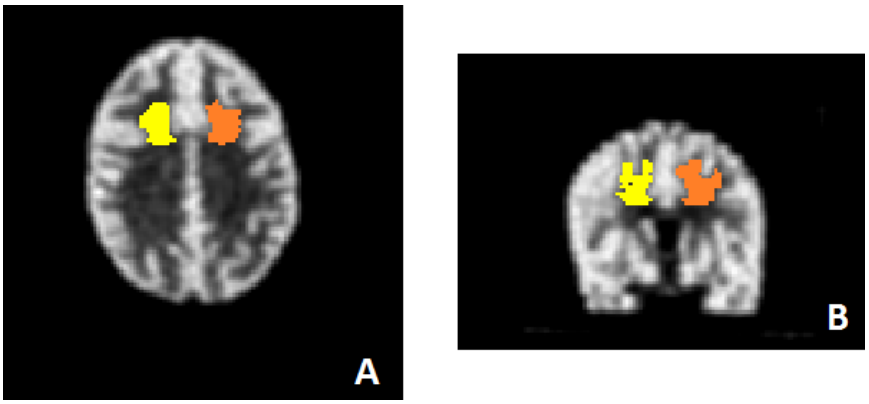

Figure 2.8: VOI for the left and right white matter (WM)

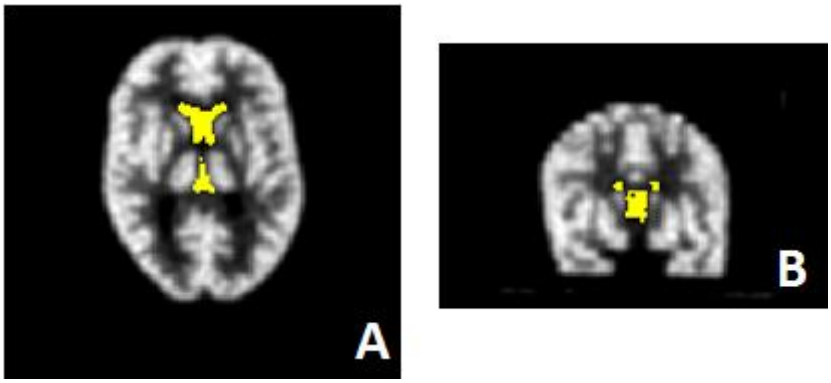

Figure 2.9: VOI for the CSF

A profile was arbitrarily drawn at position y=91 and z=55 through a transverse slice of the HBP to investigate the ratio of the grey matter to white matter (GW/WM). Along the profile generated, the peak value of the profile and the lowest value of the valley (trough) were taken. The ratio of the peak to trough was used as a measure of contrast. Graphs were then generated demonstrating the influence of different number of iterations on GW/WM ratio, for the different algorithms. Another set of graphs was generated to compare the effect of the different algorithms on counts, with a constant number of 30 iterations.

2.8. Patient data analysis

A profile was made through the transaxial slice for each of the patients. Peak and trough counts were used to obtain the peak/trough ratios (grey matter/white matter) from each reconstruction algorithm used. This ratio is a measure of contrast.

Chapter 3: Results

3.1. Hoffman brain phantom

3.1.1. Effect of varying number of iterations

3.1.1.1. Effect of the number of iterations on the GM/WM ratio

The ratio between the activity in a GM region over the activity in WM for the different VOIs listed in Table 2.1 as a function of the number of iterations (for the 25 min duration) is presented in Figures 3.1 to 3.7. These graphs show for all the VOIs that the GM/WM ratio increased as the number of iterations increased and approached convergence after 15 iterations.

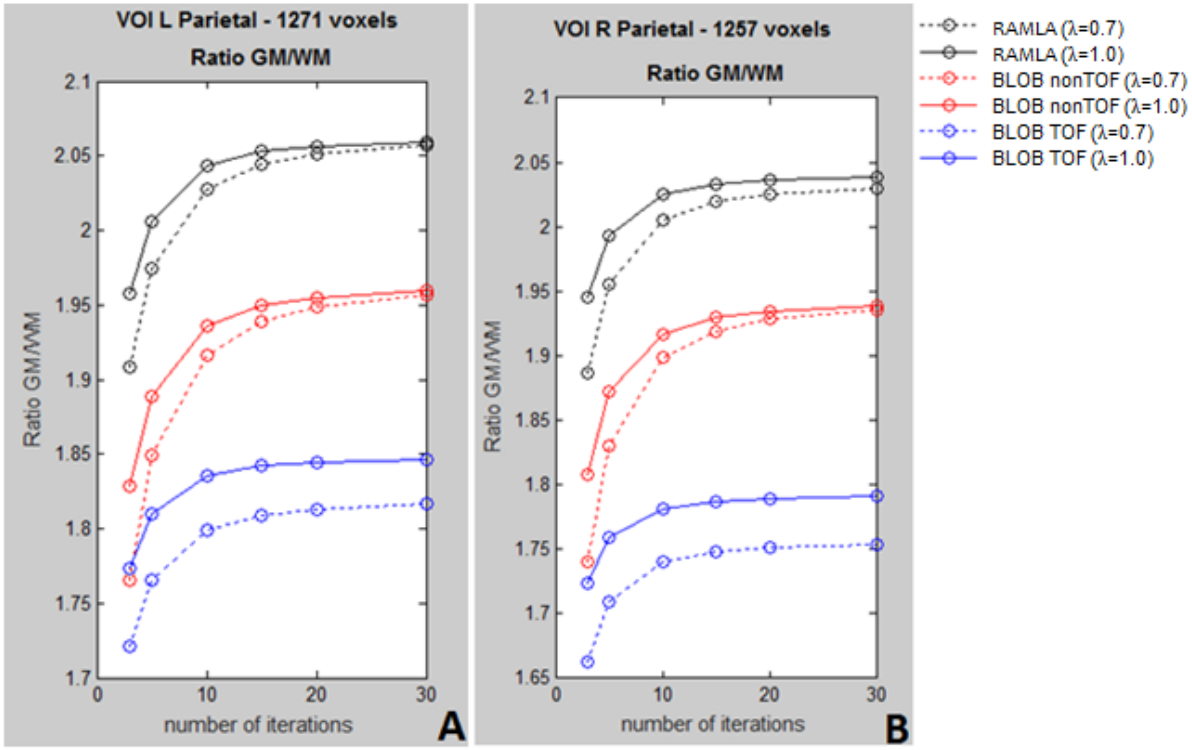

Figure 3.1: The effect of number of iterations on the GM/WM ratio for the left (A) and right (B) parietal VOIs

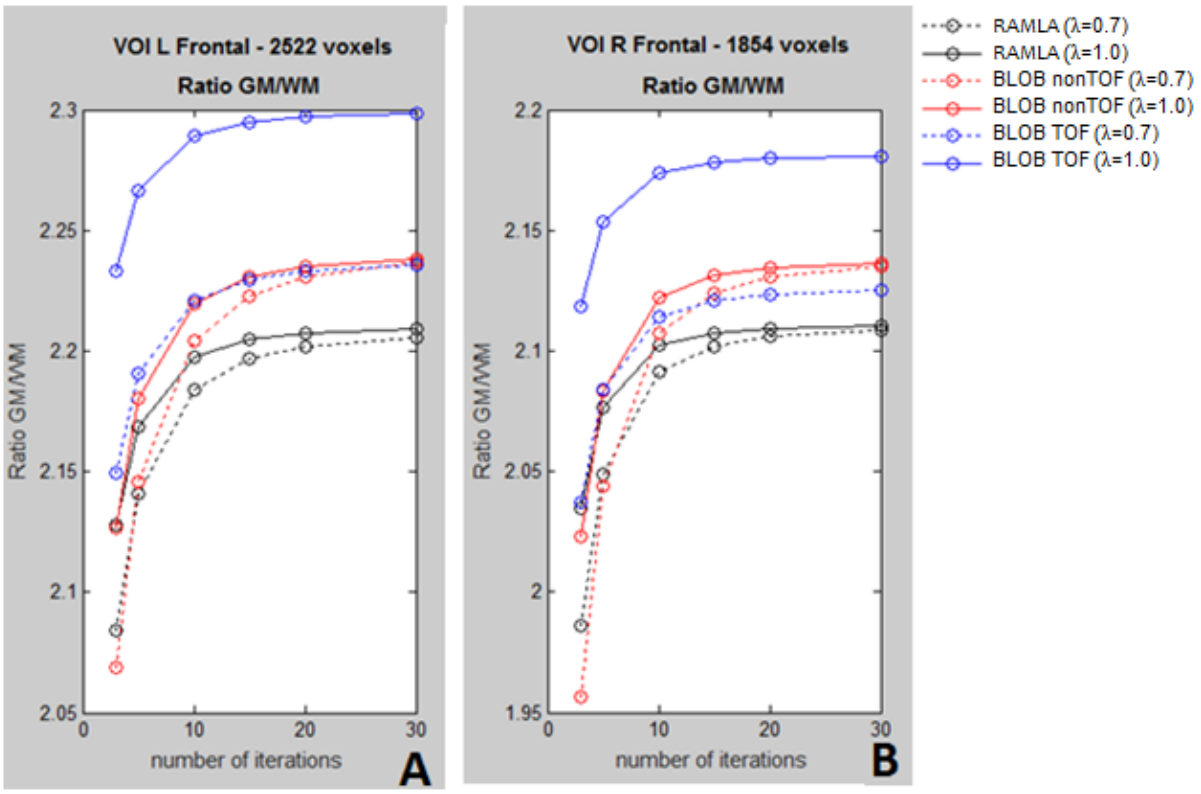

Figure 3.2: The effect of number of iterations on the GM/WM ratio for the left (A) and right (B) frontal cortex VOIs

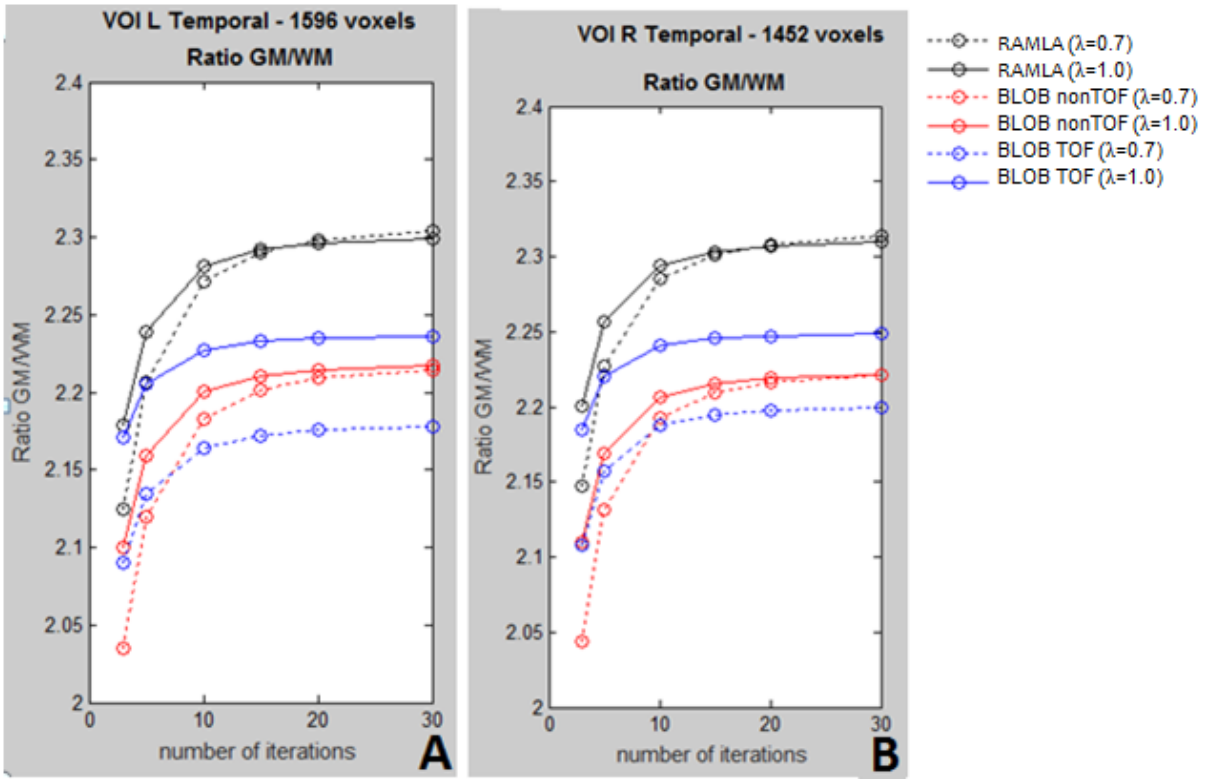

Figure 3.3: The effect of number of iterations on the GM/WM ratio for the left (A) and right (B) temporal cortex VOIs

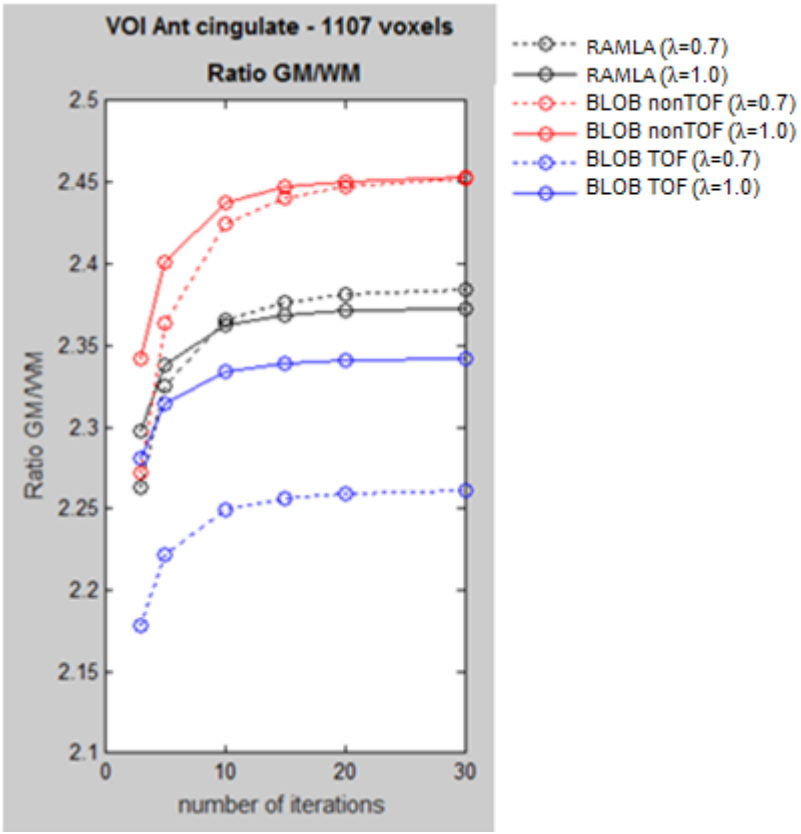

Figure 3.4: The effect of number of iterations on the GM/WM ratio for the anterior cingulate VOI

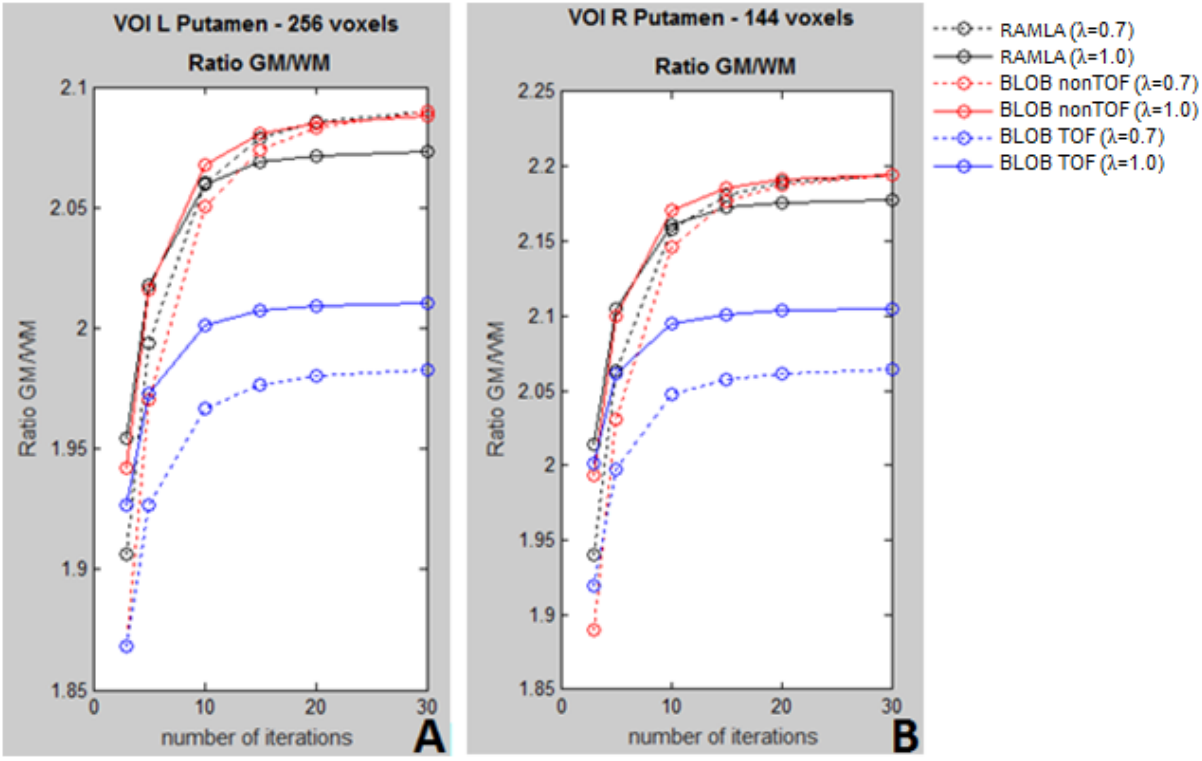

Figure 3.5: The effect of number of iterations on the GM/WM ratio for the left (A) and right (B) putamen VOIs

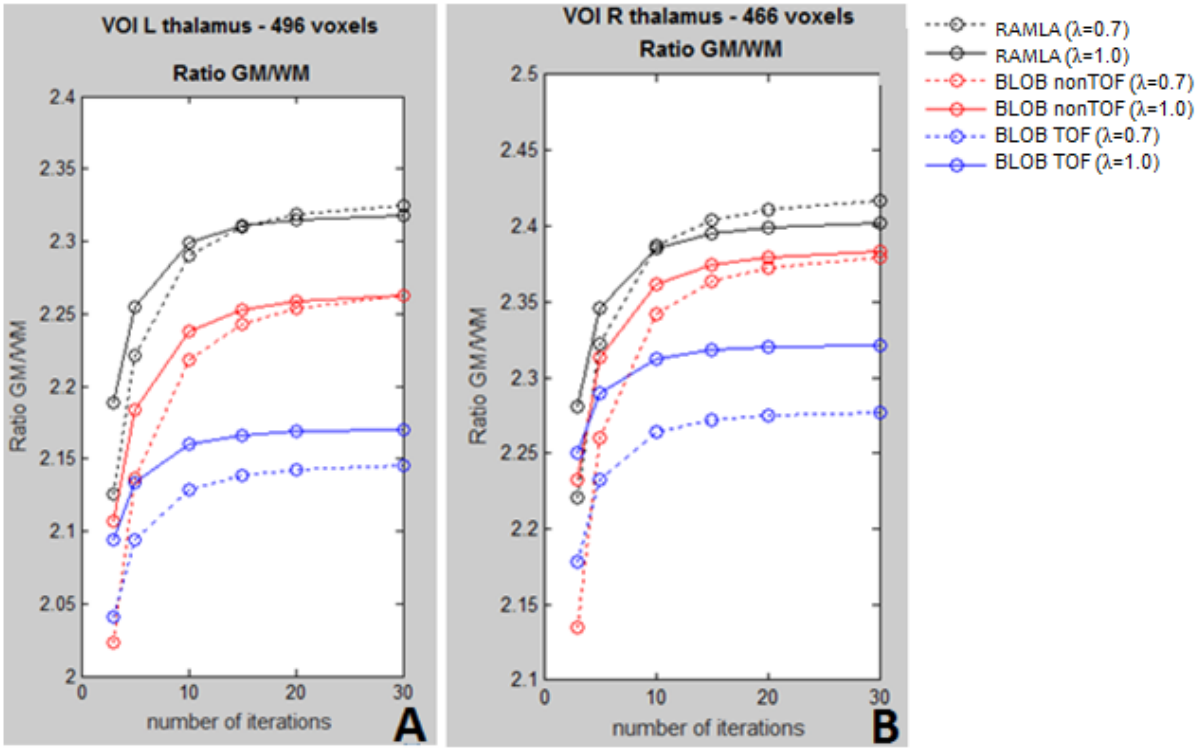

Figure 3.6: The effect of number of iterations on the GM/WM ratio for the left (A) and right (B) thalamus VOIs

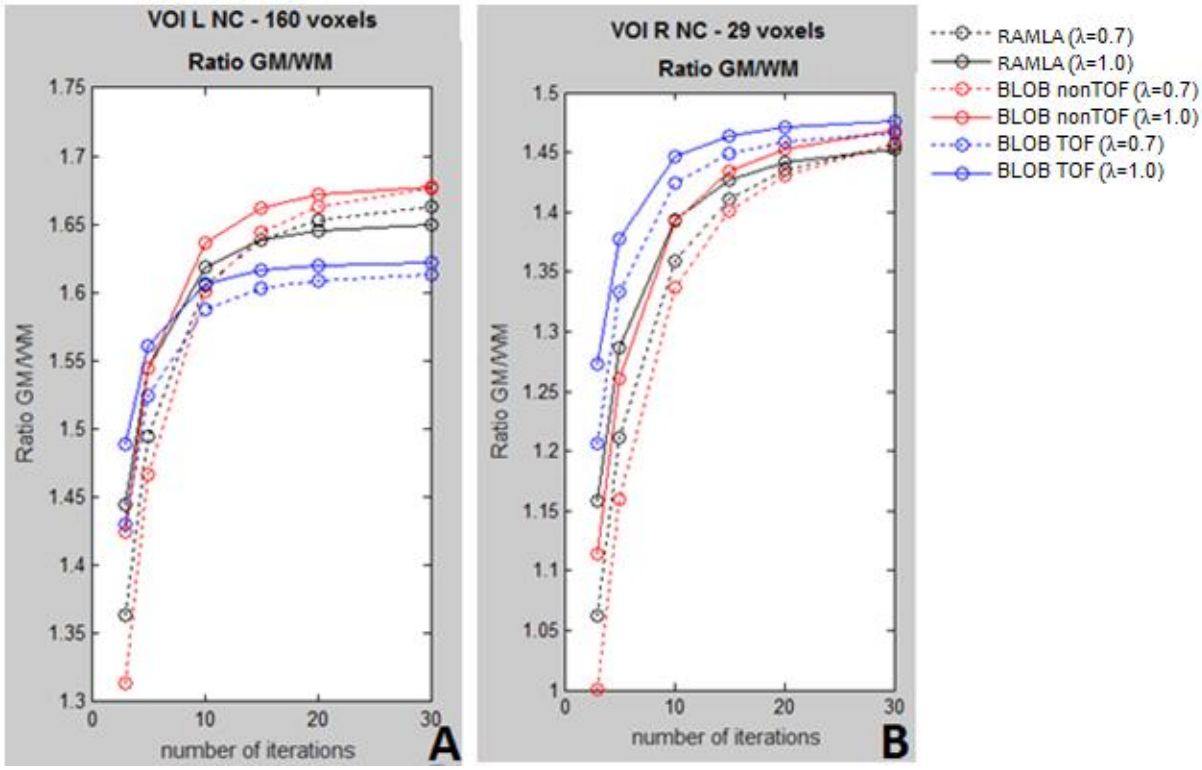

Figure 3.7: The effect of number of iterations on the GM/WM ratio for the left (A) and right (B) caudate nucleus VOIs

For most of the VOIs it was observed that convergence of the algorithms differed. BLOB TOF showed faster convergence against all the other algorithms. RAMLA showed a better contrast for most VOIs than BLOB TOF which had lower contrast. This could be because RAMLA was optimised for brain imaging on the Philips® Gemini TF Big Bore system and BLOB TOF was meant for whole body imaging with larger pixel size.

3.1.1.2. Effect of varying number of iterations on image convergence

Table 3.1 shows the convergence percentages obtained when the number of iterations was increased from 3 to 15 and from 3 to 30 iterations, and the geometric mean convergence percentage of all the VOIs. The geometric mean results confirmed that a plateau was reached after increasing the number of iterations from 3 to 15. It was found that the geometric mean of the results showed BLOB nonTOF 0.7 to have the lowest convergence of 88.4% and BLOB TOF (λ=1.0) the highest convergence of 95.7%. When comparing the algorithms with relaxation value of 0.7 and 1.0 it was found that 1.0 converged faster than 0.7. Overall, BLOB TOF (λ=1.0) proved to have faster convergence followed by BLOB TOF (λ=0.7).

Table 3.1: The convergence percentage for the GM/WM ratio between iterations 3 and 15, and between 3 and 30 for all the VOIs for all the algorithms

Iterations	VOI	RAMLA (λ=0.7)	RAMLA (λ=1.0)	BLOB nonTOF (λ=0.7)	BLOB nonTOF (λ=1.0)	BLOB TOF (λ=0.7)	BLOB TOF (λ=1.0)
3 versus 15	Left Parietal	93.4	95.5	91.2	93.8	95.0	96.1
3 versus 30		*92.7*	*95.1*	*90.2*	*93.3*	*94.8*	*96.0*
3 versus 15	Right Parietal	93.6	95.4	90.7	93.8	95.0	96.3
3 versus 30		*93.0*	*95.4*	*89.9*	*93.2*	*94.8*	*96.3*
3 versus 15	Left Frontal	94.7	96.6	93.1	95.5	96.5	97.2
3 versus 30		*94.5*	*96.3*	*92.5*	*95.0*	*96.2*	*97.1*
3 versus 15	Right Frontal	94.2	96.3	92.3	95.3	96.2	97.3
3 versus 30		*94.2*	*96.4*	*91.6*	*94.7*	*95.9*	*97.1*
3 versus 15	Left Temporal	93.0	95.1	92.7	95.0	96.2	97.2
3 versus 30		*92.2*	*94.8*	*91.9*	*94.7*	*96.0*	*97.1*
3 versus 15	Right Temporal	93.3	95.5	92.5	94.8	96.1	97.1
3 versus 30		*92.8*	*95.3*	*92.0*	*95.0*	*95.9*	*97.2*
3 versus 15	Ant Cingulate	95.1	96.7	93.0	95.6	96.6	97.5
3 versus 30		*94.9*	*96.8*	*92.7*	*95.4*	*96.3*	*97.4*
3 versus 15	Left Putamen	91.9	94.7	90.2	92.9	94.6	96.0
3 versus 30		*91.2*	*94.3*	*89.4*	*93.0*	*94.2*	*95.9*
3 versus 15	Right Putamen	89.0	92.5	86.9	91.0	92.3	95.2
3 versus 30		*88.4*	*92.5*	*86.1*	*90.8*	*93.0*	*95.1*
3 versus 15	Left Thalamus	92.0	94.8	90.1	93.7	95.4	96.5
3 versus 30		*91.4*	*94.4*	*89.4*	*93.1*	*95.2*	*96.5*
3 versus 15	Right Thalamus	92.3	95.2	90.1	93.9	96.0	97.1
3 versus 30		*91.8*	*95.0*	*89.7*	*93.6*	*95.7*	*97.0*
3 versus 15	L Caudate Nucleus	83.0	88.5	79.7	86.0	89.2	92.1
3 versus 30		*82.0*	*87.6*	*78.2*	*84.9*	*88.7*	*91.8*
3 versus 15	R Caudate Nucleus	75.1	81.3	71.4	78.1	83.5	86.7
3 versus 30		*72.9*	*79.7*	*68.6*	*75.9*	*82.3*	*86.2*
3 versus 15	***Geo Mean***	**90.6**	**93.6**	**88.4**	**92.1**	**94.0**	**95.7**
3 versus 30	***Geo Mean***	***90.0***	***93.2***	***87.6***	***91.6***	***93.7***	***95.4***

3.1.1.3. Effect of varying number of iterations on mean counts, normalised mean counts and the COV

The results of the effect of varying number of iterations on the mean counts, normalised mean counts and COV, for the VOIs used, are presented in Figures 3.8 to 3.11 for the

cortical regions, Figures 3.12 to 3.14 for the subcortical regions, and figures 3.15 and 3.16 for the white matter and CSF, respectively.

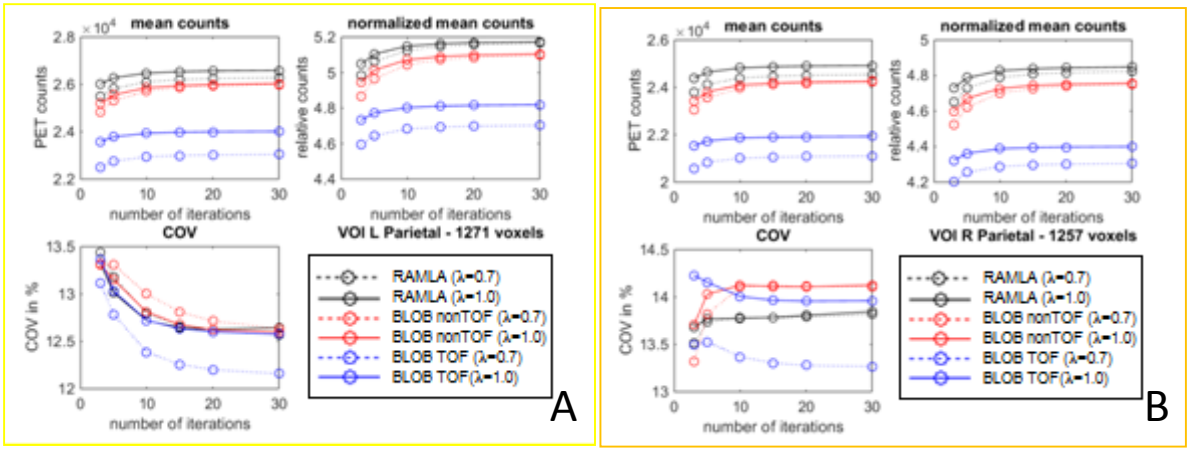

Figure 3.8: The effect of number of iterations on the mean counts; normalised mean counts and COV for the left (A) and right (B) parietal cortex

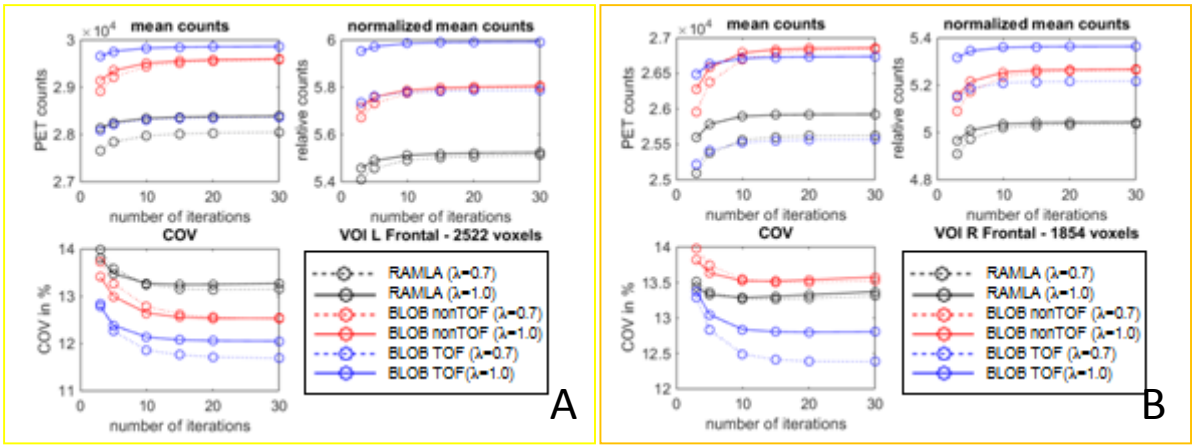

Figure 3.9: The effect of number of iterations on the mean counts; normalised mean counts and COV for the left (A) and right (B) frontal cortex

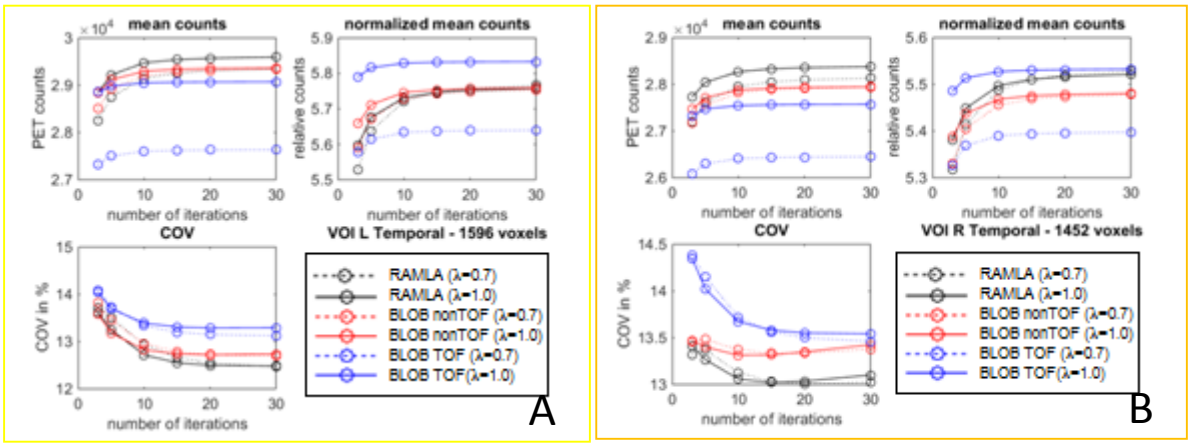

Figure 3.10: The effect of number of iterations on the mean counts; normalised mean counts and COV for the left (A) and right (B) temporal cortex

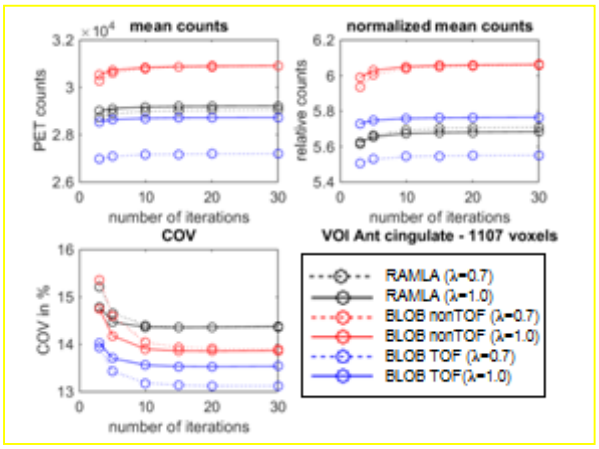

Figure 3.11: The effect of number of iterations on the mean counts; normalised mean counts and COV for the anterior cingulate

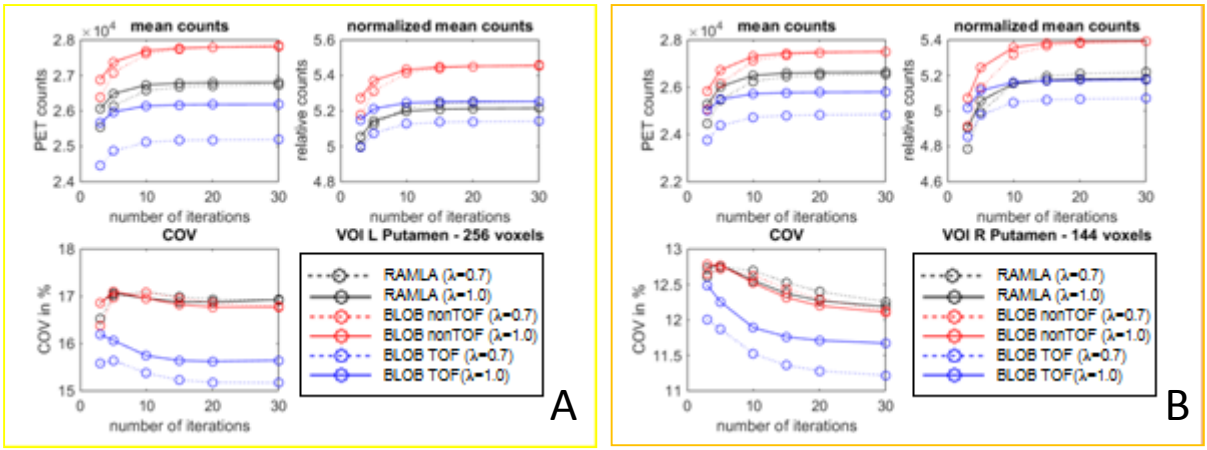

Figure 3.12: The effect of number of iterations on the mean counts; normalised mean counts and COV for the left (A) and right (B) putamen

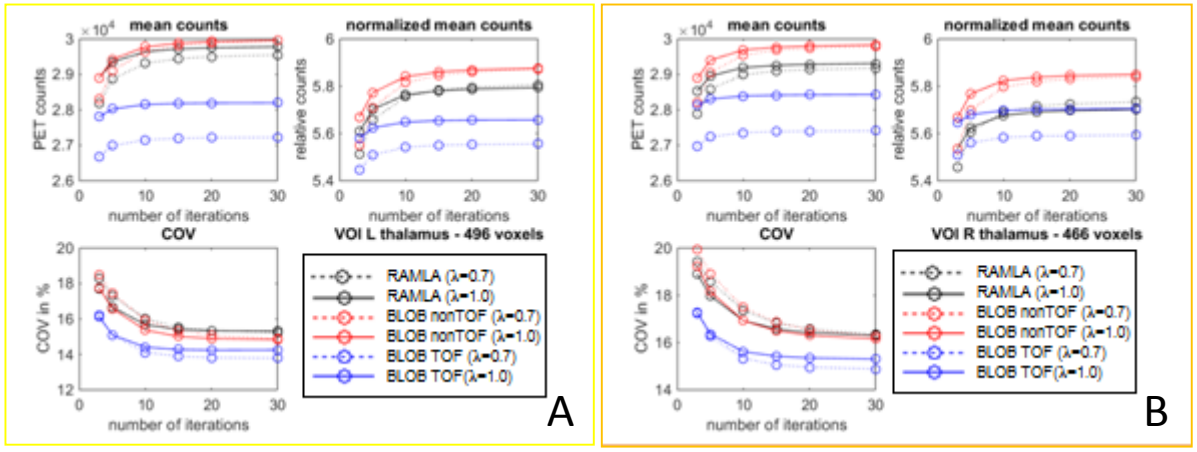

Figure 3.13: The effect of number of iterations on the mean counts; normalised mean counts and COV for the left (A) and right (B) thalamus

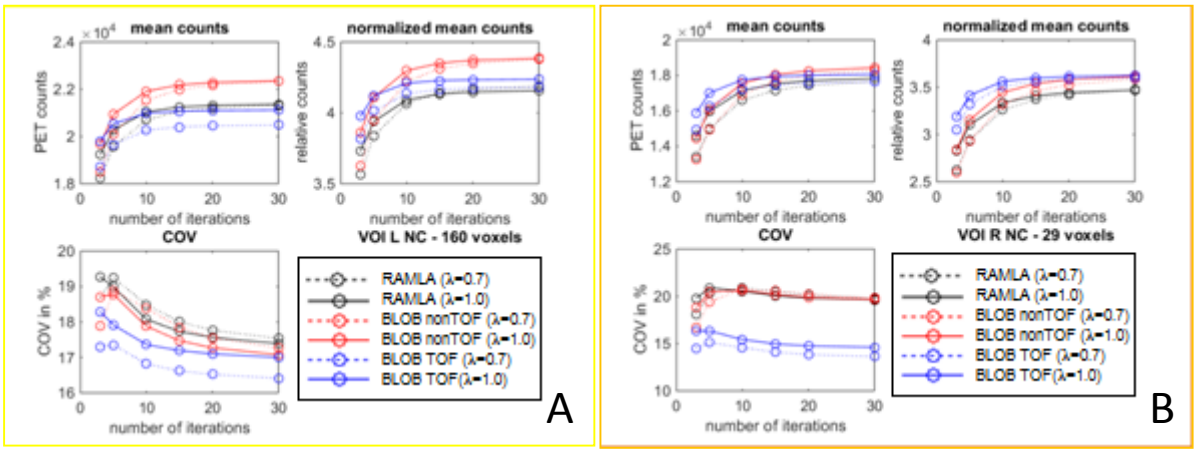

Figure 3.14: The effect of number of iterations on the mean counts; normalised mean counts and COV for the left (A) and right (B) caudate nucleus

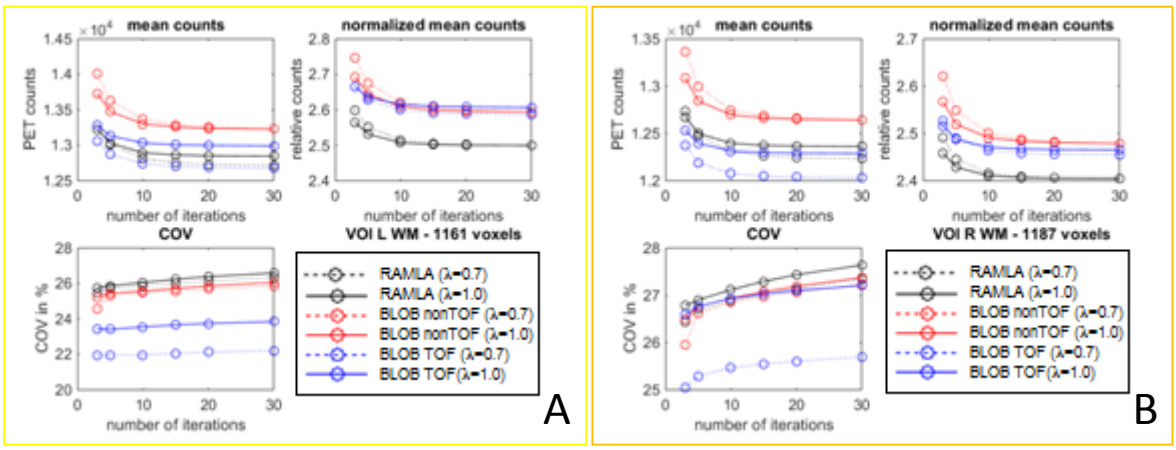

Figure 3.15: The effect of number of iterations on the mean counts; normalised mean counts and COV for the left (A) and right (B) white matter

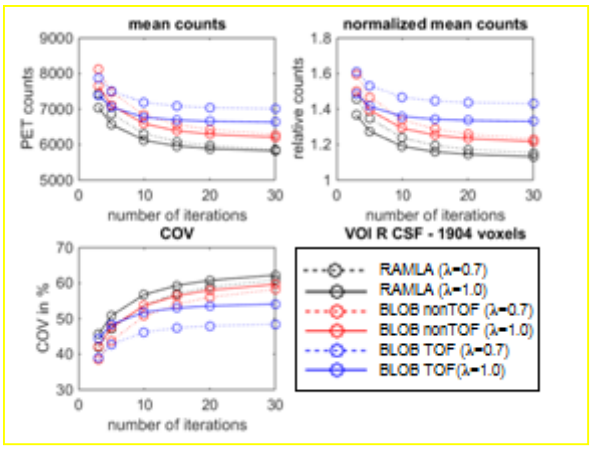

Figure 3.16: The effect of number of iterations on the mean counts; normalised mean counts and COV for the CSF

From Figures 3.8 to 3.14, it is observed that, as the number of iterations increased, the mean counts and the normalised mean counts increased and converged to a plateau

after the 15th iteration for all the cortical and subcortical structures. The COV for all VOIs showed BLOB TOF to be superior to all the other algorithms, except for the left and right temporal cortex where RAMLA is superior to BLOB TOF. BLOB TOF 0.7 appears to be superior to BLOB TOF 1.0 for most VOIs.

Figure 3.15 (for the white matter) shows that the mean counts and normalised mean counts had a maximum variation of 5.1% between 3 and 15 iterations, but from 15 to 30 iterations there was stabilisation of both the mean and normalised mean counts for all the reconstructions, with variation tending to 0%. The COV on the left and right white matter VOIs showed the BLOB TOF (λ=0.7) reconstruction to be superior followed closely by the BLOB TOF (λ= 1.0) compared to all the other reconstructions.

Figure 3.16 shows that mean counts and normalised mean counts for the CSF had a maximum variation of 19.2% up to 15 iterations and stabilised from 15 iterations on for all the reconstructions. The COV on the CSF VOIs showed BLOB TOF (λ=0.7) to be superior compared to all the other reconstructions.

3.1.2. Effect of noise by varying scan duration on mean counts, normalised mean counts and the COV

The results of the effect of varying noise by varying scan duration on the mean counts, normalised mean counts and COV, are presented in Figures 3.17 to 3.20 for the cortical regions, Figures 3.21 to 3.23 for the subcortical regions, and Figures 3.24 and 3.25 for the white matter and CSF, respectively.

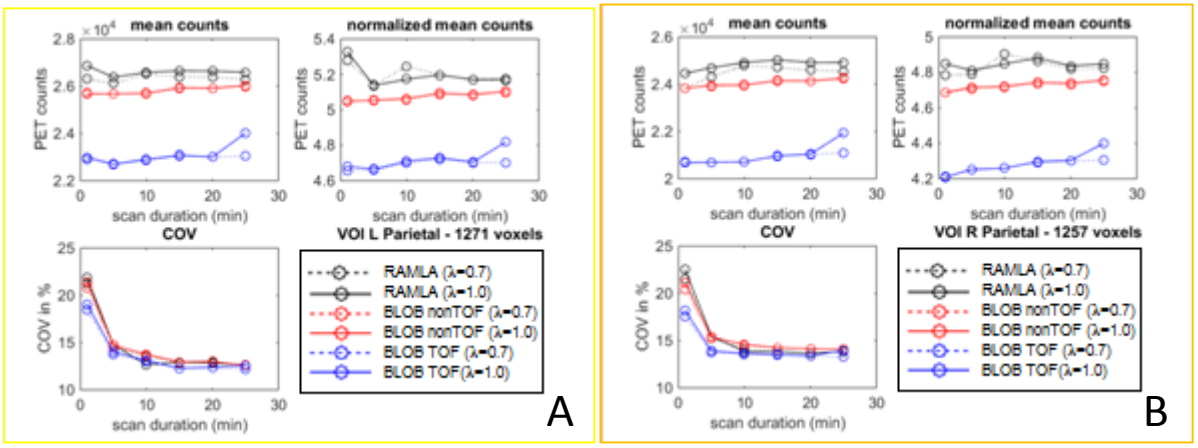

Figure 3.17: The effect of noise by varying scan duration on the mean counts; normalised mean counts and COV for the left (A) and right (B) parietal cortex

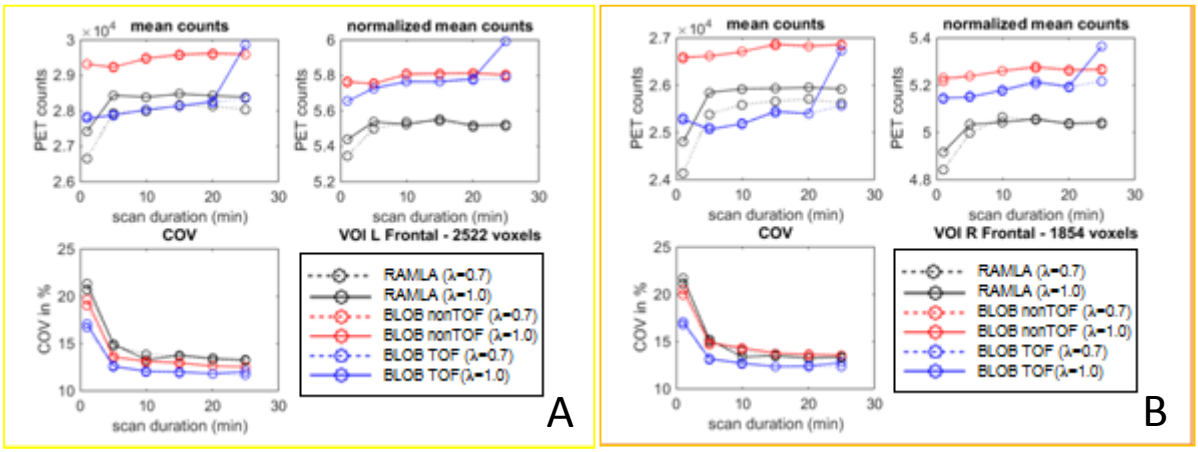

Figure 3.18: The effect of noise by varying scan duration on the mean counts; normalised mean counts and COV for the left (A) and right (B) frontal cortex

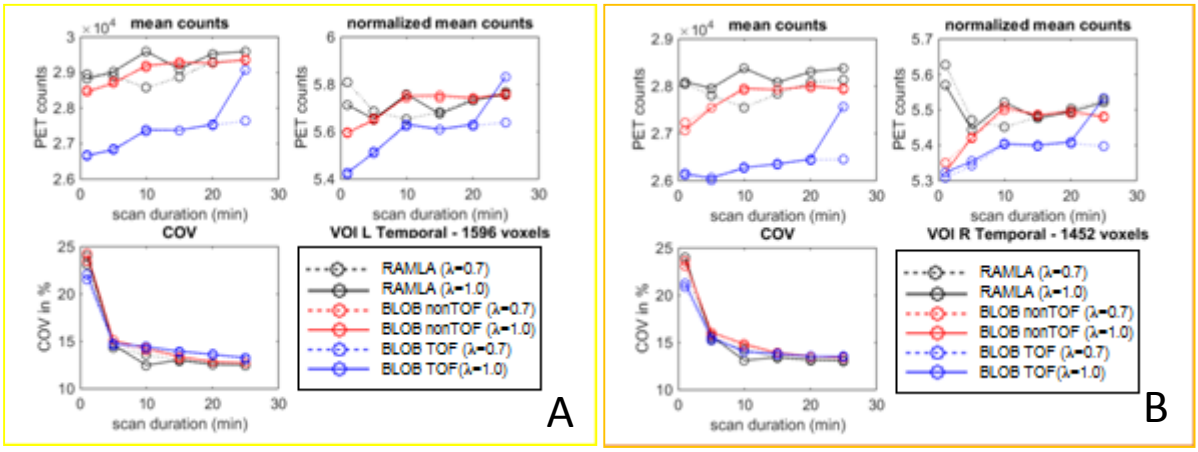

Figure 3.19: The effect of noise by varying scan duration on the mean counts; normalised mean counts and COV for the left (A) and right (B) temporal cortex

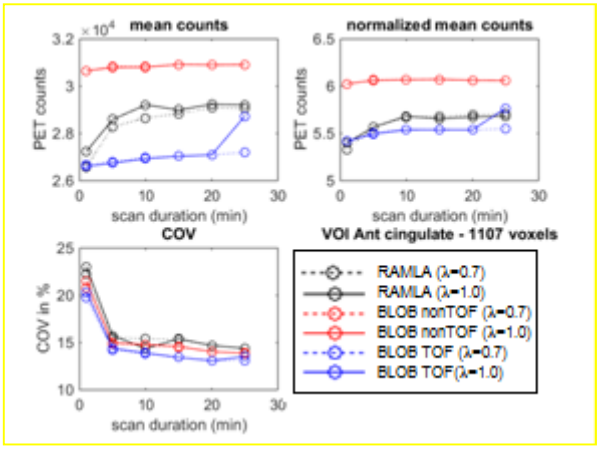

Figure 3.20: The effect of noise by varying scan duration on the mean counts; normalised mean counts and COV for the anterior cingulate

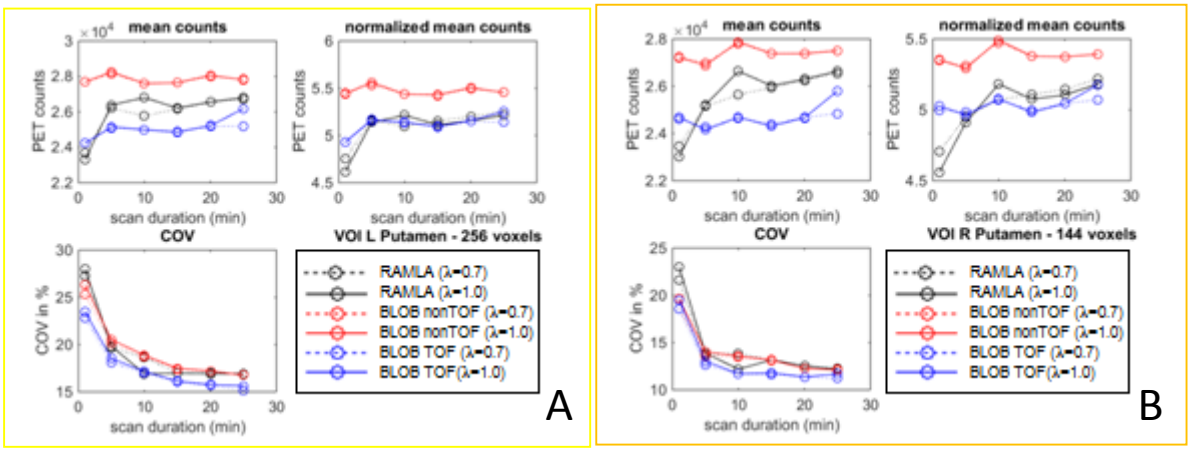

Figure 3.21: The effect of noise by varying scan duration on the mean counts; normalised mean counts and COV for the left (A) and right (B) putamen

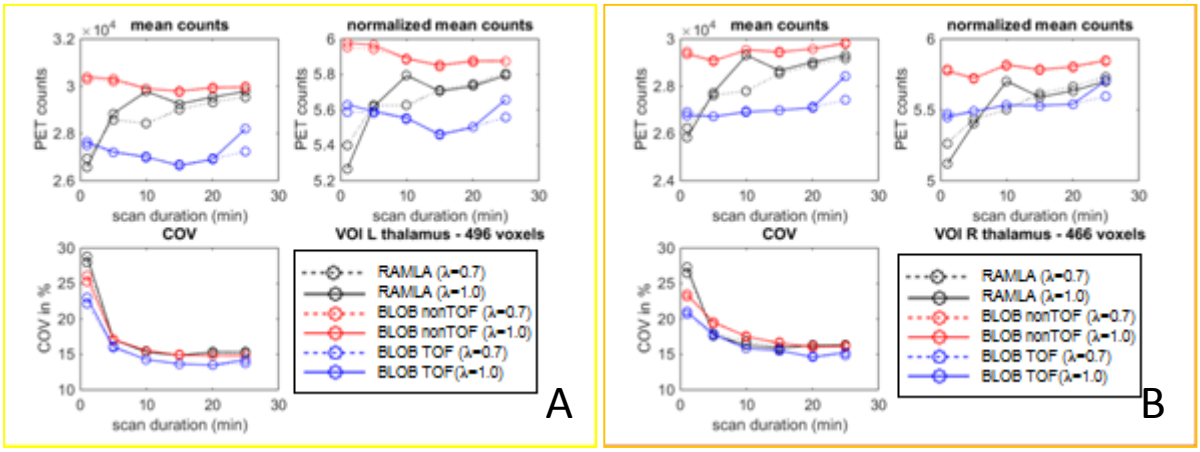

Figure 3.22: The effect of noise by varying scan duration on the mean counts; normalised mean counts and COV for the left (A) and right (B) thalamus

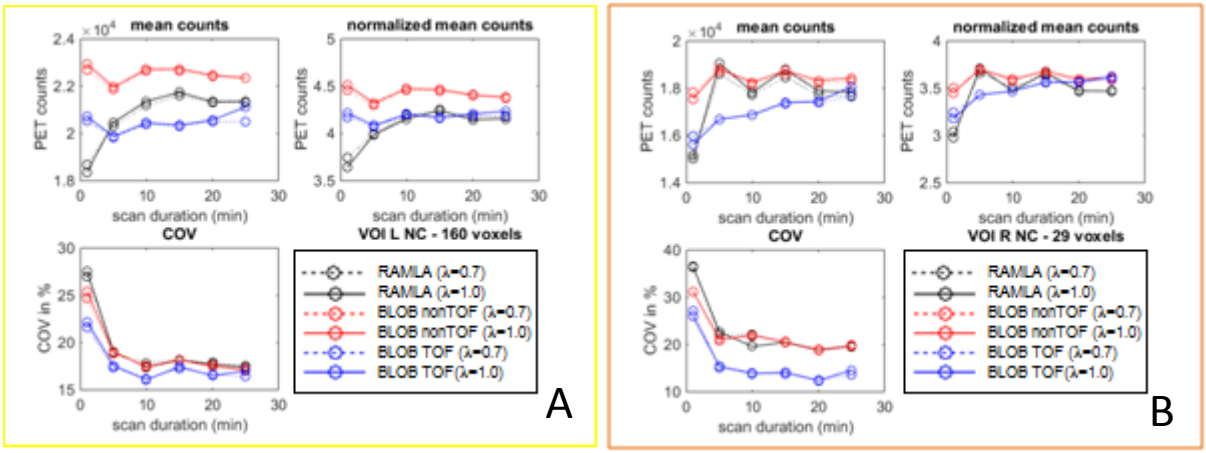

Figure 3.23: The effect of noise by varying scan duration on the mean counts; normalised mean counts and COV for the left (A) and right (B) caudate nucleus

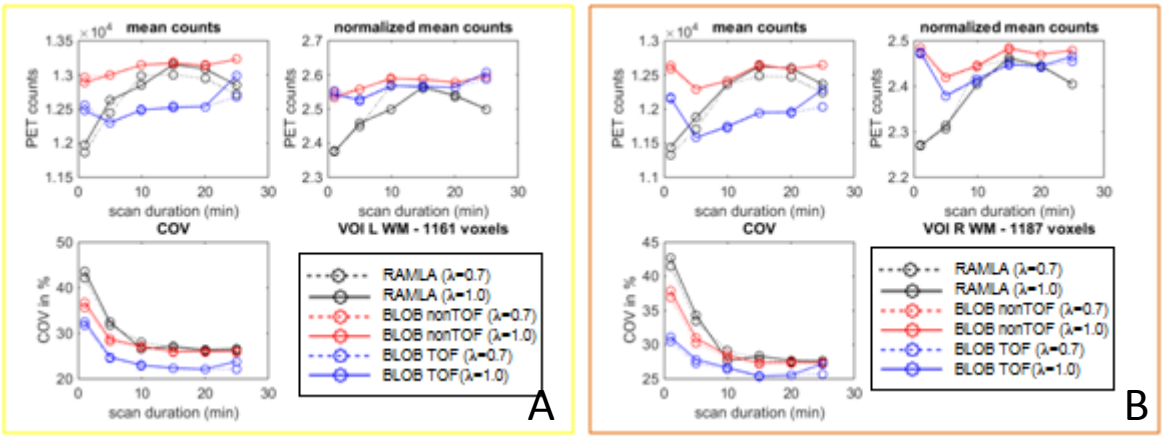

Figure 3.24: The effect of noise by varying scan duration on the mean counts; normalised mean counts and COV for the left (A) and right (B) white matter

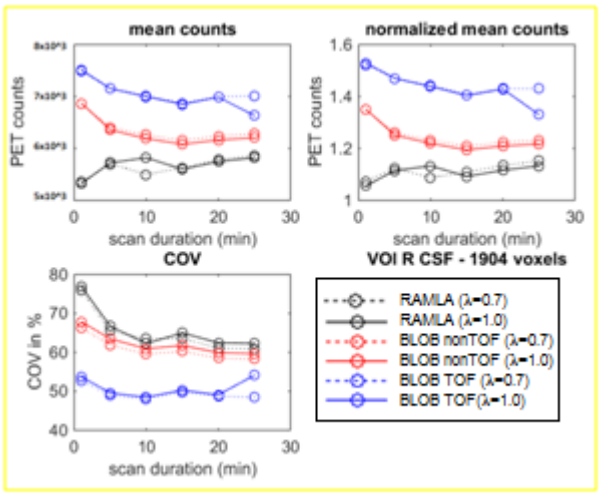

Figure 3.25: The effect of noise by varying scan duration on the mean counts; normalised mean counts and COV for the CSF

Figures 3.17 to 3.20 show that the mean counts and normalised mean counts of the cortical regions for the BLOB nonTOF and BLOB TOF were comparatively stable irrespective of noise, with the exception of very short scan durations where there was very high noise. The only algorithm that showed a higher variation compared to the rest was RAMLA, which showed the highest variation of 5.2%. The COV curves showed an improvement as the noise decreased (scan duration increased) with stability reached from 10 min. COV for all VOIs showed BLOB TOF to be superior to all the other algorithms, except for the left and right temporal cortex, where RAMLA showed slight competitive superiority to BLOB TOF in the low noise region.

In Figure 3.21 to 3.23, it is shown that the mean counts and normalised mean counts of the subcortical regions for the BLOB nonTOF and BLOB TOF were fairly stable irrespective of noise for all the VOIs compared, except for RAMLA which showed the

highest variation of 13.2% compared to other reconstructions. The COV curves showed an improvement as the noise decreased and reached stability from 10 min with no further significant improvement up to 25 min. BLOB TOF appeared to be superior as the noise decreased for all VOIs compared to all the other algorithms.

For the white matter, Figure 3.24 shows that the mean counts and normalised mean counts of the RAMLA had the highest variation of 15% compared to other reconstructions. The COV on the white matter VOIs showed the BLOB TOF to be superior compared to all the other reconstructions. The COV graph showed improvement as the noise decreased and reached stability from 10 min with no further significant improvement up to 25 min.

Figure 3.25 shows that the mean counts and normalised mean counts of all the algorithms for the CSF were fairly stable irrespective of noise. The COV showed the BLOB TOF to be superior and improving as the noise decreased and reached stability from 10 min with no further significant improvement up to 25 min when compared to all the other reconstructions.

3.1.3 Profile along the Hoffman brain phantom slice

Figure 3.26 shows the position of the profile drawn across the transverse plane of the Hoffman brain phantom at y = 91 z = 55.

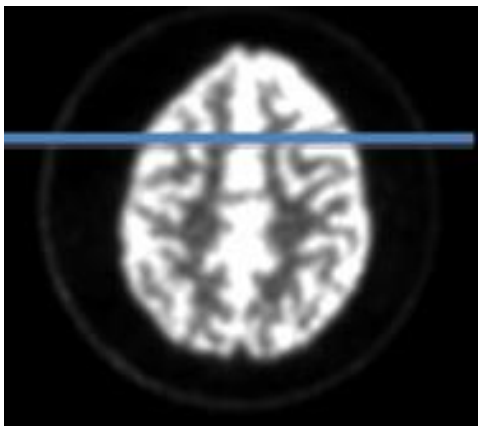

Figure 3.26: Profile along the transverse plane on the slice of the HBP

Figure 3.27 A-F demonstrates the HBP profiles for the different algorithms for the lowest and highest number of iterations. Increasing the number of iterations appears to improve contrast.

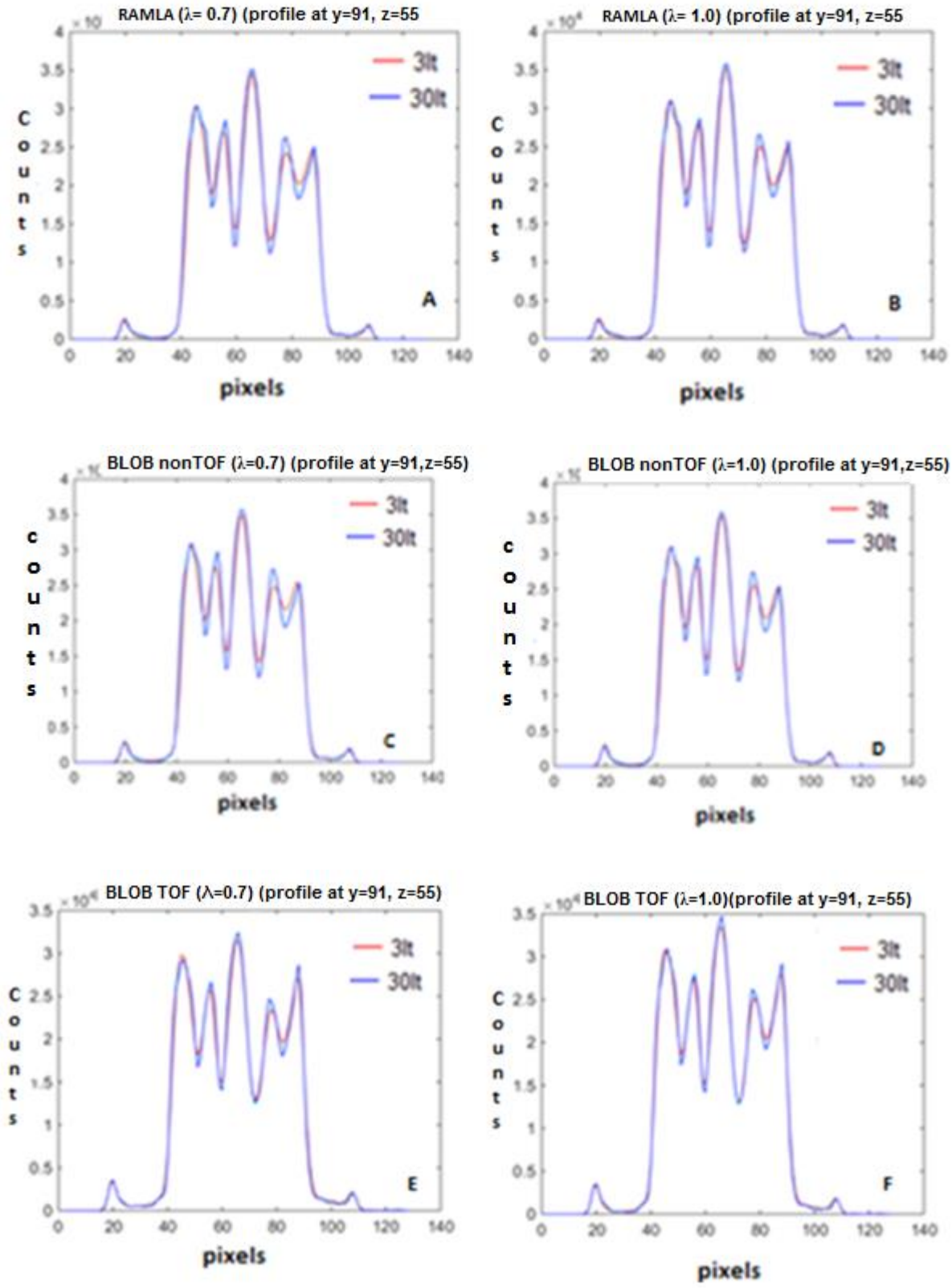

Figure 3.27: The profile curve obtained from the Hoffman brain phantom for each algorithm for different number of iterations

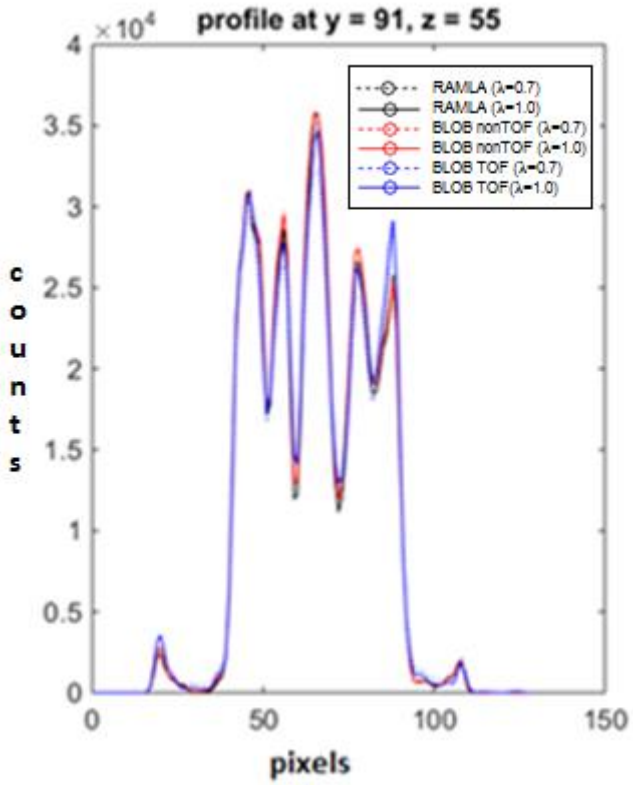

Figure 3.28.: The profile curve obtained from the Hoffman brain phantom reconstructed with different algorithms

Figure 3.28 showed that BLOB TOF generally showed higher values than the other reconstruction algorithms.

3.2. Patient brain data results

Fourteen patients that were referred to the PET/CT Centre for normal whole body PET/CT scanning were initially identified, but only eight of these qualified according to the inclusion and exclusion criteria. Of these, three patients withdrew and one scan failed the quality control, therefore only three patients were included. This low recruitment turnout was due to the strict inclusion and exclusion criteria.

3.2.1. Patient data

Figure 3.29 shows a bar graph of the ratios of geometric means of grey matter (peak) and white matter (trough) for the three patients, obtained from a profile drawn through a representative slice of each brain image. This ratio represents the contrast in the profile lines. The figure illustrates the effect of different algorithms, also comparing the effect of lambda (smooth (λ=0.7) and normal (λ=1.0)). It was noted that there was a variation with no pattern between the three patients therefore no conclusion could be deduced.

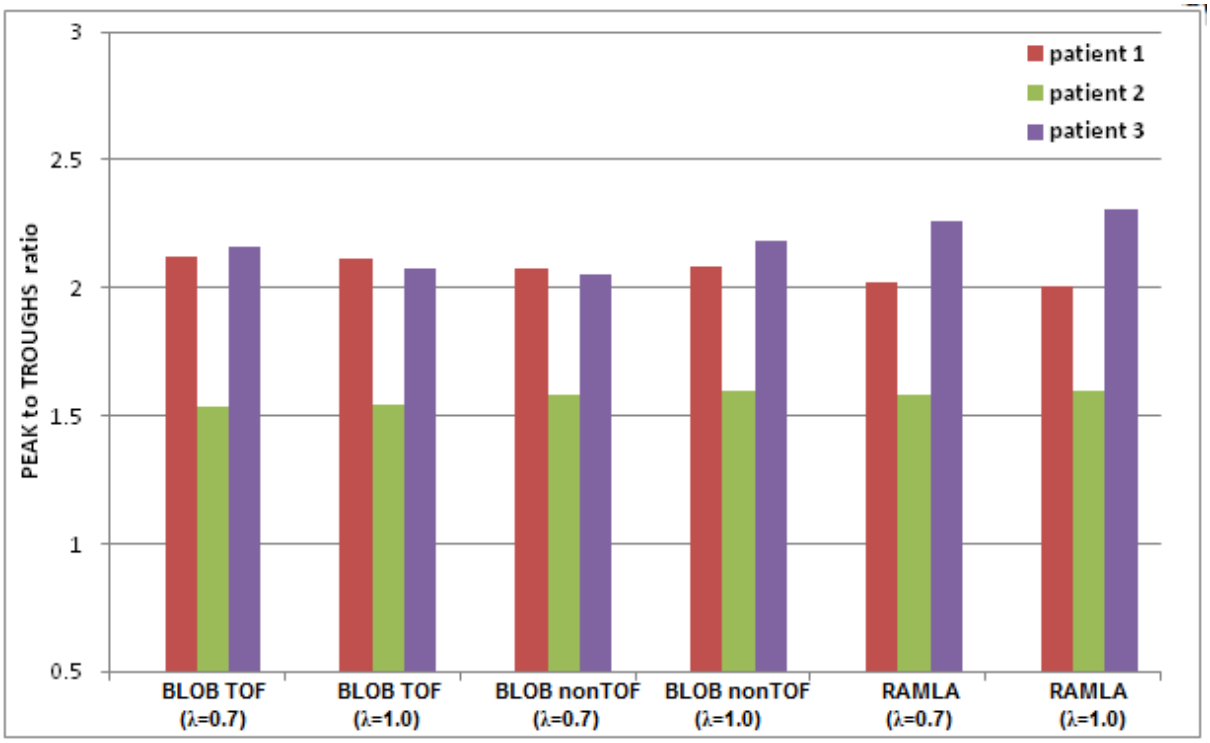

Figure 3.29: Bar plot of the peak to troughs ratio in the profile lines for patient brain images

3.2.2. Profile along patient brain slice

Figure 3.30 is an illustrative example of the data of a profile drawn over slice y= 91 z= 55. It shows the counts obtained when the profile was drawn for the various algorithms while varying the number of iterations. Figure 3.31 shows the effect of different algorithms on the profile. No specific trend was observed.

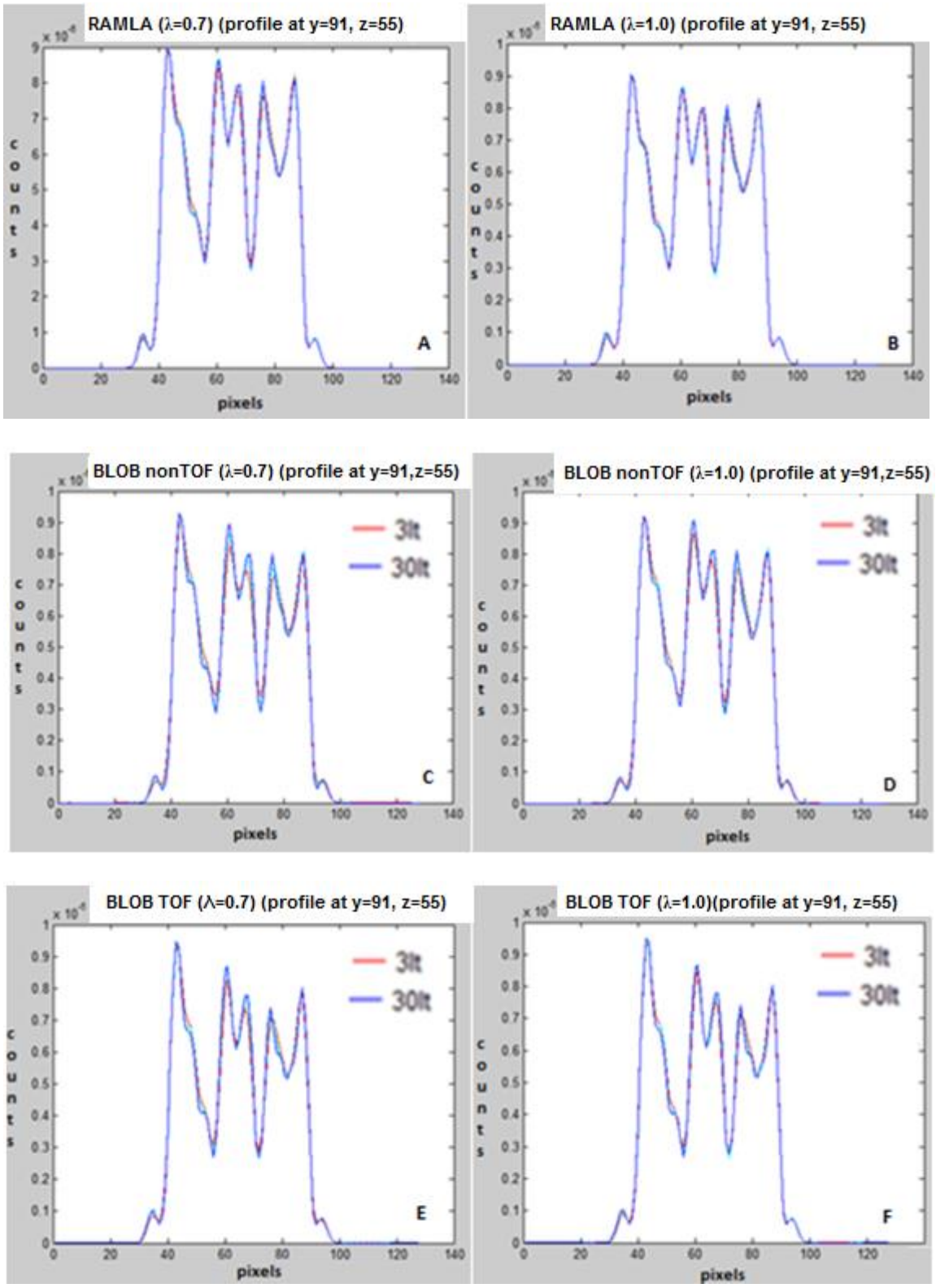

Figure 3.30: The profile curve obtained from the data of patient 1 for each algorithm for different number of iterations

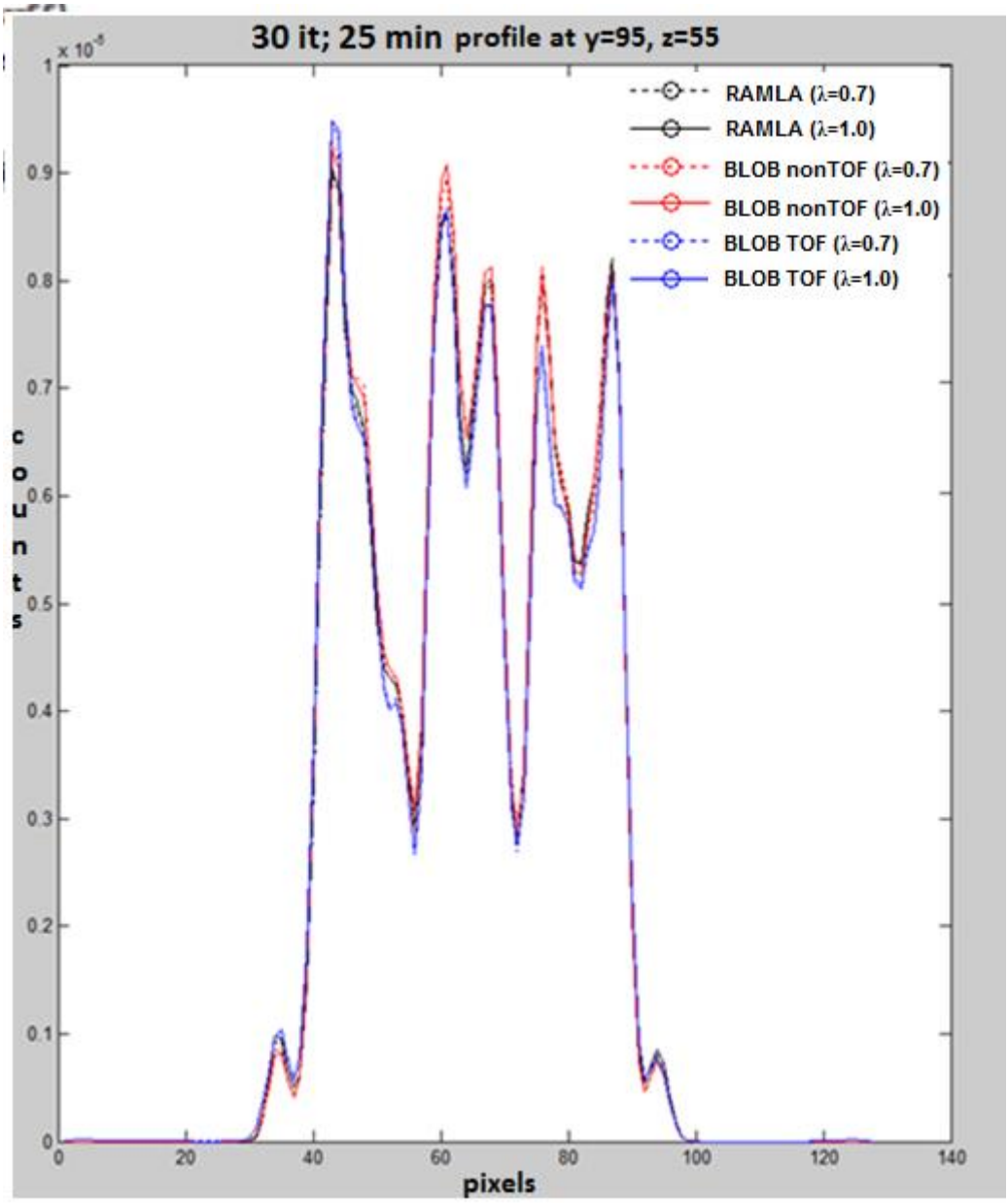

Figure 3.31: The profile curve obtained from the patient data 1 reconstructed with different algorithms

Due to the limited number of patients and the variation in the results obtained, the data was not analysed further. Further studies need to be conducted including more patients.

Chapter 4: Discussion

This research was conducted to evaluate the effect of different processing algorithms on PET/CT image quality, specifically to optimise PET/CT brain imaging. Various parameters were investigated, including the number of iterations, relaxation parameter (λ), and scan duration. The inclusion of time of flight information was also studied.

4.1. Number of iterations

When investigating the effect of varying the number of iterations, the acquisition time was kept constant at 25 min while different algorithms with different values of lambda were applied. For the GM/WM ratio, it was found that it increased as the number of iterations increased, with convergence reached from the 15th iteration onward (Figures 3.1-3.7). Iterations beyond 15 resulted in minimal improvement of accuracy. COV also showed stability from 15 iterations onwards in cortical regions (Figures 3.8-3.11) and sub-cortical regions (Figures 3.12-3.14). For WM and CSF (Figures 3.15 and 3.16), COV was higher but also stabilised after 15 iterations. Therefore, using 15 iterations is a good compromise between reaching convergence while maintaining an acceptable reconstruction time. This is in contrast to other studies where the number of iterations for optimal image quality was less than 15. The studies reviewed, used 12 or less iterations for image reconstruction (Leemans *et al*., 2015; Prieto *et al*., 2015; Zeimpekis *et al*., 2015). None of these studies concluded on the optimal number of iterations required for optimum image quality for brain.

Similarly, it was found that most of the algorithms reached stability from the 15th iteration onwards when evaluating the effect that varying the number of iterations had on mean and normalised mean counts (Figures 3.8-3.16). This result is in agreement with the findings of Matej and Lewitt (1996), who stated that a number of iterations from 10 and above would lead to results close to the expected standard. It however, contradicts Conti (2011) who stated that the number of iterations for clinical applications should not exceed 10. It is important to note that Conti's work was done on a Biograph block-detector PET/CT system (Siemens®), analysing whole-body imaging data which have lower count statistics compared to brain imaging data. Increasing the number of iterations increases computation time, hence the need to determine the optimum number of iterations required for an acceptable trade off between image quality and processing time specifically for brain imaging. The results of this study showed that 15 iterations led to optimal brain image quality, but more than

15 iterations (up to 30) did not show a significant difference in image quality (Table 3.1).

4.2. Relaxation parameters

BLOB TOF (λ=1.0) convergence was shown to be superior to BLOB TOF (λ=0.7) and to all the other algorithms, as expected from the iteration formula (Table 3.1). This is in concordance with Groheux *et al*. (2009), who also found that larger λ values accelerated the convergence speed.

When evaluating the effect of the relaxation parameter, for most of the VOIs, excluding the temporal cortex, the BLOB TOF (λ=0.7) appeared to give lower COV compared to that of all the other algorithms (Figures 3.8-3.16). This is in agreement with the findings by Groheux *et al*. (2009) who stated that increasing lambda would result in increased noise which can directly affect accuracy. A direct comparison of our results with that of Groheux *et al* (2009) could not be done as different PET scanners and different lambda values were used.

The results of the COV for the temporal regions appear to be different from all other VOIs, as RAMLA was superior to the other algorithms. The cause of this is unclear, and needs to be investigated further.

When choosing the lambda value a balance must be found to avoid choosing too small or too large values, in order to avoid too smooth or too noisy images.

4.3. Scan times

The study also investigated the effect of noise by varying the scan duration while applying a constant number of 30 iterations. As scan duration increased, there was a decrease in noise. In turn, as the noise decreased, the COV for all the algorithms showed an improvement (Figures 3.17-3.25). In regions of high noise, the BLOB TOF COV started off better (lower) compared to the other algorithms. As the noise decreased by increasing scan duration, all the algorithms converged to a low COV with BLOB TOF being superior to all the others (Figure 3.17-3.25). This finding is supported by Westerwoudt, Conti and Eriksson (2014), who stated that the use of TOF information has the beneficial effect of lowering the statistical limitations and allowing for shorter reliable PET scans. The COV results for different scan durations show that there was minimal improvement after 5 min in high-activity regions (GM) and after 10 min in low-activity regions (WM). According to Zeimpekis *et al*. (2015), the average overall PET/CT image quality of the brain at 10 min is excellent. In their study, they

evaluated image quality as a function of acquisition time in a new TOF PET/MRI compared to TOF PET/CT. In the current study an image acquisition of 10 min produced an optimal trade-off between image quality and scan duration for brain imaging irrespective of the reconstruction algorithm used.

4.4. Time of flight information

This study also found that the incorporation of time of flight information in the reconstruction enhanced convergence. BLOB TOF 1.0 had faster convergence overall against all the other algorithms (Table 3.1).

For the COV percentage, the quality of the PET brain phantom reconstructed with the BLOB TOF was superior to that of BLOB nonTOF and RAMLA (Figures 3.8-3.16). This is in agreement with a study by Taniguchi *et al.* (2015), who found that the inclusion of the OSEM+TOF+PSF improved image quality.

The mean counts of the BLOB TOF overall were lower than that of the RAMLA and BLOB nonTOF algorithms (Figures 3.8-3.16). This can be due to the fact that RAMLA was optimised for brain imaging with 2 mm pixel size, while BLOB TOF was optimised for whole body imaging with a 4 mm pixel size.

As was found with the relaxation parameter λ, the results of the COV for the temporal regions (Figures 3.10) appear to be different from all other VOIs, with RAMLA superior to the other algorithms. The cause of this is unclear, and needs to be investigated further.

4.5. Patient data

The scan data of a limited number of patients showed discordant results when compared to the brain phantom data (Figures 3.29-3.30). To confirm these preliminary findings, a more representative sample of patient data needs to be studied. Due to the low patient inclusion rate this was not possible within the time frame of this study. Therefore, while showing these preliminary findings, it is not possible to interpret their significance.

Chapter 5: Conclusions

The following conclusions can be drawn from the findings of this study:

- Fifteen iterations gave an optimal image quality for most algorithms.
- BLOB TOF gave an optimal COV, with λ=0.7 giving better accuracy than λ=1.0. This is because reducing the lambda value decreases the noise generated, thereby improving image quality. The incorporation of time of flight information in the reconstruction enhanced convergence, with BLOB TOF (λ=1.0) being superior to BLOB TOF (λ=0.7) and all other algorithms. This is because BLOB TOF (λ=1.0) has a larger lambda value which leads to faster convergence. When choosing between BLOB TOF (λ=0.7) and (λ=1.0) it is important to choose an optimal value in order to avoid over smooth or over noisy images within an acceptable processing time.
- The acquisition time for an optimal trade-off between image quality and scan time for brain imaging was 10 min.
- For the GM/WM ratio, RAMLA had the best contrast. This can be due to the fact that RAMLA was optimised for brain imaging with 2 mm pixel size, while BLOB TOF was optimised for whole body imaging with a 4 mm pixel size. Further research by optimising BLOB TOF to a comparable pixel size (2 mm) needs to be done.

A representative sample of sufficient patient data will need to be studied to validate the phantom data with statistical analysis on a voxel basis.

The study hypothesis that optimisation of different image reconstruction parameters, and the inclusion of TOF in the reconstruction algorithm will improve the image quality of brain images on the Philips® PET/CT scanner, was confirmed.

Further research

The current algorithm used for brain imaging on the Phillips® system is RAMLA which uses a 2 mm pixel size. The BLOB TOF algorithm which is optimised for whole body imaging uses 4 mm pixel size. Therefore, the resolution of images reconstructed using RAMLA is better than those reconstructed with BLOB TOF. Optimisation of the BLOB TOF algorithm by altering the blob size to a comparable pixel size of 2 mm could potentially improve the spatial resolution, thereby reducing the partial volume effect and improving the resolution and contrast of BLOB TOF. Future research is required

to compare the image parameters of RAMLA and BLOB TOF using comparable pixel sizes in order to determine the optimal reconstruction algorithm for brain PET/CT.

The choice between BLOB TOF (λ=0.7) and (λ=1.0) needs to balance image smoothness and noisiness within an acceptable computation time. Further research to find an optimal lambda value is also needed.

Studies using an appropriate sample of human subjects need to be done in order to validate these findings in a clinical setting.

Bibliography

Akamatsu, G., Ishikawa, K., Mitsumoto, K., Taniguchi, T., Ohya, N., Baba, S., Abe, K. and Sasaki, M., 2012. Improvement in PET/CT image quality with a combination of point-spread function and time-of-flight in relation to reconstruction parameters. *Journal of Nuclear Medicine*, *53*(11), pp.1716-1722.

Akamatsu, G., Mitsumoto, K., Taniguchi, T., Tsutsui, Y., Baba, S. and Sasaki, M., 2014. Influences of point-spread function and time-of-flight reconstructions on standardized uptake value of lymph node metastases in FDG-PET. *European Journal of Radiology*, *83*(1), pp.226-230.

Basu, S., Kwee, T.C., Surti, S., Akin, E.A., Yoo, D. and Alavi, A., 2011. Fundamentals of PET and PET/CT imaging. *Annals of the New York Academy of Sciences*, *1228*(1), pp.1-18.

Browne, J. and De Pierro, A.B., 1996. A row-action alternative to the EM algorithm for maximizing likelihood in emission tomography. *IEEE Transactions on Medical Imaging*, *15*(5), pp.687-699.

Bushberg, J.T., Seibert, J.A., Leidholdt, E.M. and Boone, J.M., 2002. *The Essential Physics of Medical Imaging. 2nd ed,* Phildelphia: Lippincott Williams and Wilkins.

Cherry, S.R., Sorenson, J.A and Phelps, M.E., 2012. *Physics in Nuclear Medicine.* 4th ed. Philadelphia: Elsevier Saunders, p.327.

Chuang, K., Jan, M., Wu, J., Lu, J., Chen, S., Hsu, C. and Fu, Y., 2005. A maximum likelihood expectation maximization algorithm with thresholding. *Computerized Medical Imaging and Graphics*, *29*(7), pp.571-578.

Conti, M., 2009. State of the art and challenges of time-of-flight PET. *Physica Medica*, *25*(1), pp.1-11.

Conti, M., 2011. Focus on time-of-flight PET: the benefits of improved time resolution. *European Journal of Nuclear Medicine and Molecular Imaging*, *38*(6), pp.1147-1157.

Daube-Witherspoon, M.E., Matej, S., Karp, J.S. and Lewitt, R.M., 2001. Application of the row action maximum likelihood algorithm with spherical basis functions to clinical PET imaging. *IEEE Transactions on Nuclear Science*, 48(1), pp.24-30.

Daube-Witherspoon, M.E., Zubal, I.G. and Karp, J.S., 2003. Developments in instrumentation for emission computed tomography. *Seminars in Nuclear Medicine*, 33(1), pp.28-41.

Groheux, D., Martineau, A., Vrigneaud, J.M., Hindie, E., Baillet, G. and Moretti, J.L., 2009. Effect of variation in relaxation parameter value on LOR-RAMLA reconstruction of 18F-FDG PET studies. *Nuclear Medicine Communications*, *30*(12), pp.926-933.

Henkin, R.E., Bova, D., Dillehay, G.L., Karesh, SM., Halama, J.R., Wagner, J.H., 2006. *Nuclear Medicine*, 2nd ed, Philadelphia: Mosby Elsevier, pp.271-292.

Herman, G.T. and Meyer, L.B., 1993. Algebraic reconstruction techniques can be made computationally efficient [positron emission tomography application]. *IEEE Transactions on Medical Imaging*, *12*(3), pp.600-609.

Hu, Z., Wang, W., Gualtieri, E.E., Hsieh, Y.L., Karp, J.S., Matej, S., Parma, M.J., Tung, C.H., Walsh, E.S., Werner, M. and Gagnon, D., 2007. An LOR-based fully-3D PET image reconstruction using a blob-basis function. *IEEE Nuclear Science Symposium Conference Record* Vol. 6, pp.4415-4418.

Kadrmas, D.J., Casey, M.E., Conti, M., Jakoby, B.W., Lois, C. and Townsend, D.W., 2009. Impact of time-of-flight on PET tumor detection. *Journal of Nuclear Medicine*, *50*(8), pp.1315-1323.

Kadrmas, D.J., Oktay, M.B., Casey, M.E. and Hamill, J.J., 2012. Effect of scan time on oncologic lesion detection in whole-body PET. *IEEE Transactions on Nuclear Science*, *59*(5), pp.1940-1947.

Karp, J.S. and Fletcher, J.W., 2006. Time of flight PET. *SNM PET Center of Excellence Newsletter,* 3(4), pp.1-4.

Karp, J.S., Surti, S., Daube-Witherspoon, M.E. and Muehllehner, G., 2008. Benefit of time-of-flight in PET: experimental and clinical results. *Journal of Nuclear Medicine*, *49*(3), pp.462-470.

Leemans, E.L., Kotasidis, F., Wissmeyer, M., Garibotto, V. and Zaidi, H., 2015. Qualitative and quantitative evaluation of blob-based time-of-flight PET image reconstruction in hybrid brain PET/MR imaging. *Molecular Imaging and Biology*, *17*(5), pp.704-713.

Lewellen, T. and Karp, T., 2004. PET Systems. *Emission Tomography (The fundamentals of PET and SPECT).* USA: Elsevier Science, pp.179-194.

Lonsdale, M.N. and Beyer, T., 2010. Dual-modality PET/CT instrumentation - today and tomorrow. *European Journal of Radiology*, *73*(3), pp.452-460.

Matej, S. and Lewitt, R.M., 1996. Practical considerations for 3-D image reconstruction using spherically symmetric volume elements. *IEEE Transactions on Medical Imaging*, *15*(1), pp.68-78.

Mittra, E. and Quon, A., 2009. Positron emission tomography/computed tomography: the current technology and applications. *Radiologic Clinics of North America*, *47*(1), pp.147-160.

Nagaki, A., Onoguchi, M. and Matsutomo, N., 2014. Clinical validation of high-resolution image reconstruction algorithms in brain 18F-FDG-PET: effect of incorporating Gaussian filter, point spread function, and time-of-flight. *Nuclear Medicine Communications*, *35*(12), pp.1224-1232.

Popescu, L.M., Matej, S. and Lewitt, R.M, 2004. Iterative image reconstruction using geometrically ordered subsets with list-mode data. *Nuclear Science Symposium Conference Record,* 6, pp.3536-3540.

Prieto, E., Martí-Climent, J.M., Morán, V., Sancho, L., Barbés, B., Arbizu, J. and Richter, J.A., 2015. Brain PET imaging optimization with time of flight and point spread function modelling. *Physica Medica*, *31*(8), pp.948-955.

Saha, G.B., 2010. Cyclotron and Production of PET Radionuclides. *Basics of PET Imaging*, pp.117-130. New York: Springer.

Smith, N.B. and Webb, A., 2011. Introduction to medical imaging. In: M. W. Saltzman & S. Chien, eds. *Physics, Engineering and Clinical Applications.* USA: Cambridge University Press, pp.24-35.

Spinks, T.J., 2000. PET Theory. In: Lindon, J.C., Tranter, G.E., Holmes, J.L. eds., 2000. *Encyclopedia of Spectroscopy and Spectrometry*: O-Z. Cambridge (Ma): Elsevier. pp.1782-1791.

Suljic, A., Tomse, P., Jensterle, L. and Skrk, D., 2015. The impact of reconstruction algorithms and time of flight information on PET/CT image quality. *Radiology and Oncology*, *49*(3), pp.227-233.

Surti, S., Karp, J.S. and Kinahan, P.E., 2004. PET instrumentation. *Radiologic Clinics of North America*, *42*(6), pp.1003-1016.

Surti, S., Kuhn, A., Werner, M.E., Perkins, A.E., Kolthammer, J. and Karp, J.S., 2007. Performance of Philips Gemini TF PET/CT scanner with special consideration for its time-of-flight imaging capabilities. *Journal of Nuclear Medicine*, *48*(3), pp.471-480.

Taniguchi, T., Akamatsu, G., Kasahara, Y., Mitsumoto, K., Baba, S., Tsutsui, Y., Himuro, K., Mikasa, S., Kidera, D. and Sasaki, M., 2015. Improvement in PET/CT image quality in overweight patients with PSF and TOF. *Annals of Nuclear Medicine*, *29*(1), pp.71-77.

Tarantola, G., Zito, F. and Gerundini, P., 2003. PET instrumentation and reconstruction algorithms in whole-body applications. *Journal of Nuclear Medicine*, *44*(5), pp.756-769.

Townsend, D.W., 2008. Positron emission tomography/computed tomography. *Seminars in Nuclear Medicine* 38(3), pp.152-166.

Turkington, T.G., 2001. Introduction to PET instrumentation. *Journal of Nuclear Medicine Technology*, *29*(1), pp.4-11.

Vandenberghe, S., D'Asseler, Y., Van de Walle, R., Kauppinen, T., Koole, M., Bouwens, L., Van Laere, K., Lemahieu, I. and Dierckx, R.A., 2001. Iterative reconstruction algorithms in nuclear medicine. *Computerized Medical Imaging and Graphics*, *25*(2), pp.105-111.

Varrone, A., Asenbaum, S., Vander Borght, T., Booij, J., Nobili, F., Någren, K., Darcourt, J., Kapucu, Ö.L., Tatsch, K., Bartenstein, P. and Van Laere, K., 2009. EANM procedure guidelines for PET brain imaging using [18F] FDG, version 2. *European Journal of Nuclear Medicine and Molecular Imaging*, *36*(12), pp.2103-2110.

Wang, W., Hu, Z., Gualtieri, E.E., Parma, M.J., Walsh, E.S., Sebok, D., Hsieh, Y.L., Tung, C.H., Song, X., Griesmer, J.J. and Kolthammer, J.A., 2006. Systematic and distributed time-of-flight list mode PET reconstruction. *IEEE Nuclear Science Symposium Conference Record* 3, pp.1715-1722

Westerwoudt, V., Conti, M. and Eriksson, L., 2014. Advantages of improved time resolution for TOF PET at very low statistics. *IEEE Transactions on Nuclear Science*, *61*(1), pp.126-133.

Wilson, J.M. and Turkington, T.G., 2013. TOF-PET small-lesion image quality measured over a range of phantom sizes. *IEEE Transactions on Nuclear Science*, *60*(3), pp.1589-1595.

Zeimpekis, K., Huellner, M., Barbosa, F.D.G., Ter Voert, E., Davison, H., Delso, G. and Veit-Haibach, P., 2015. Clinical evaluation of PET image quality as a function of acquisition time in a new TOF-PET/MRI compared to TOF-PET/CT-initial results. *Molecular Imaging and Biology*, 17(5), pp.735-744

Zeng, L., Nuyts, J. and De Man, B., 2007. Statistical methods for image reconstruction, MIC 2007 Short Course. [PowerPoint presentation]. *Statistical methods for image reconstruction*. Lecture III: X-Ray CT Iterative Reconstruction. Honolulu, 30 October. Available from: http://slideplayer.com/slide/9733219/ [Accessed 09 October 2015].